JGR Space Physics

RESEARCH ARTICLE
10.1029/2025JA034094

Studying the Evolution of ICMEs in the Heliosphere Through Multipoint Observations

Zhiyong Zhang[1], Chenglong Shen[1,2], Yutian Chi[3], Dongwei Mao[4], Junyan Liu[4], Mengjiao Xu[3], Zhihui Zhong[4], Jingyu Luo[4], Can Wang[4], and Yuming Wang[1,2,5]

[1]Deep Space Exploration Laboratory/School of Earth and Space Sciences, University of Science and Technology of China, Hefei, China, [2]CAS Center for Excellence in Comparative Planetology, University of Science and Technology of China, Hefei, China, [3]Deep Space Exploration Laboratory, Institute of Deep Space Sciences, Hefei, China, [4]CAS Key Laboratory of Geospace Environment, Department of Geophysics and Planetary Sciences, University of Science and Technology of China, Hefei, China, [5]Anhui Mengcheng Geophysics National Observation and Research StationUniversity of Science and Technology of China, Mengcheng, China

Key Points:

- The decay rate of the magnetic field and the expansion rate of the radius of interplanetary coronal mass ejection (ICMEs) are slightly lower than the self-similar expansion
- The axial magnetic flux and helicity can be considered to be conserved during ICME propagation
- The difference in magnetic pressure and velocity between the ICME and the solar wind is the major factor affecting the ICME expansion

Correspondence to:
C. Shen,
clshen@ustc.edu.cn

Citation:
Zhang, Z., Shen, C., Chi, Y., Mao, D., Liu, J., Xu, M., et al. (2025). Studying the evolution of ICMEs in the heliosphere through multipoint observations. *Journal of Geophysical Research: Space Physics*, *130*, e2025JA034094. https://doi.org/10.1029/2025JA034094

Received 20 APR 2025
Accepted 23 JUN 2025

Abstract Interplanetary coronal mass ejections (ICMEs) are the main cause of severe space weather in near-Earth space. To better understand the evolution of ICMEs in interplanetary propagation, we identified 14 multipoint observed ICME events via various lists of ICMEs, which confirmed the multipoint associations previously made by other researchers for these events. We use the in situ measurements as well as model results of these 14 ICMEs to obtain the evolution of the ICMEs in interplanetary space. We found that the dependence of the average total magnetic field strength on the radial distance is $B_t \propto D^{-1.68 \pm 0.17}$. The radial dependence of the axial magnetic field strength is $B_0 \propto D^{-1.54 \pm 0.15}$. These dependencies indicate that the decay rates of the magnetic field are slightly slower than expected from self-similar expansion. The relationship between radius of the flux rope and radial distance is $R \propto D^{0.84 \pm 0.22}$, which is closed to the expectation of self-similar expansion but still slightly lower. However, for each group of ICME, their radial dependence varies significantly. Only 36% of events are basically self-similar expansions. This may be due to the effect of the magnetic pressure difference and velocity difference between an ICME and the background solar wind on the ICME expansion. In the process of ICME propagation, the axial magnetic flux and helicity can be considered essentially conserved. We also analyzed the changes in the flux rope axis orientation and found that the majority (71%) of the events changed the axis direction, and the flux rope axis tends to be horizontal and solar west-east or east-west.

1. Introduction

Coronal mass ejection is a phenomenon in which the sun ejects a large amount of magnetized plasma into interplanetary space (Aulanier, 2010; GulisanoF et al., 2012; Mierla et al., 2010; Vourlidas, 2014; J. Zhang et al., 2021). Its interplanetary counterpart is commonly referred to as interplanetary coronal mass ejection (ICME) (Chi et al., 2016; Fadaaq & Badruddin, 2021; Mustajab & Badruddin, 2011; Plunkett et al., 2001; I. G. Richardson & Cane, 2012; Russell et al., 2005; J. Zhang et al., 2021). The ICME is an important carrier of strong southward magnetic fields, and it is generally considered to be the primary interplanetary structure responsible for geomagnetic storms (Echer et al., 2008; Gonzalez et al., 1994, 2007, 2011; Wang et al., 2002; Xue et al., 2005; J. Zhang et al., 2003). The geomagnetic storm is a type of severe space weather. Strong geomagnetic storms can cause severe disturbances in the Earth's magnetosphere, ionosphere and thermosphere (Lockwood et al., 2016, 2020; Wang, Rosen, et al., 2016; Yu et al., 2021). They can also adversely affect or even paralyze navigation, communication and power transmission systems (Shen et al., 2017; Yu et al., 2023). To reduce the harm caused by ICMEs, we need to understand the evolution of ICMEs during interplanetary propagation to prepare for ICME forecasting, which is the significance of our study.

The early evolution of ICMEs is dominated by Lorentz forces, which accelerate the ICMEs and cause them to expand rapidly (Chen & Kunkel, 2010; Vršnak, 2008). As the radial distance increases, the Lorentz force decreases and is gradually ignored (Vršnak et al., 2004). In the later stage, the evolution of ICMEs is influenced mainly by the interaction between ICMEs and the background solar wind. For example, ICMEs are affected by magnetohydrodynamic drag during propagation (Cargill, 2004; Chi, Shen, Liu, et al., 2023; Shen et al., 2011, 2012, 2014; Vršnak et al., 2008, 2013), slowing down/accelerating ICMEs that are faster/slower than the background solar wind; that is, the speed of the ICMEs eventually becomes consistent with the background solar wind (Gopalswamy et al., 2000).

At present, there are two main approaches used to study the evolution of ICMEs: statistical approach and multipoint observation approach (Wang et al., 2005). The statistical method uses all the ICMEs observed by spacecraft/detectors at different locations to study the statistical relationship between the ICME parameters (magnetic field and radius) and the radial distance (Liu et al., 2005; Wang et al., 2005; Wang & Richardson, 2004). Liu et al. (2005) used in situ observation data from the Helios 1 and 2, Ulysses, Wind and Advanced Composition Explorer (ACE) spacecraft to identify ICMEs and investigate the evolution of the radial width, density, magnetic field magnitude and temperature of ICMEs during propagation. Wang et al. (2005) identified ICMEs via in situ observation data from Helios 1 and 2, Pioneer Venus Orbiter (PVO), ACE and Ulysses spacecraft and analyzed the power law relationships among ICME density, magnetic field magnitude, temperature and radial distance. The multipoint observation method uses multiple spacecraft at different locations to track labeled ICMEs and analyze the radial evolution of their parameters (Vršnak et al., 2019; Salman et al., 2020; Reisenfeld et al., 2003; Riley et al., 2003; J. D. Richardson et al., 2002; Paularena et al., 2001; McAllister et al., 1996; Gosling et al., 1995). Vršnak et al. (2019) studied the diameter, magnetic field strength, and derived axial current and axial magnetic flux as a function of the power law of the radial distance of 11 magnetic clouds observed by at least two radially aligned spacecraft. Davies et al. (2021) analyzed the dependence of the mean magnetic field strength on the radial distance for 35 ICMEs with multipoint observations and compared the evolutionary differences before and after 1 AU. Salman et al. (2020) created a catalog containing 47 multipoint observed ICMEs via in situ observation data from the Mercury Surface, Space Environment, Geochemistry and Ranging (MESSENGER), Venus Express (VEX), Solar-Terrestrial Relations Observatory (STEREO), and Wind/ACE spacecraft and analyzed the evolution of the maximum magnetic field intensity in sheaths and ejecta. The main advantage of the statistical method over the multipoint observation method is the greater number of ICME events involved.

With the advent of the space age, an increasing number of spacecraft/probes have been launched into space, performing missions at different radial distances. The increasing number of spacecraft/probes in the heliosphere provides more multipoint observation events with smaller longitude differences for studying the evolution of ICMEs. In this study, we utilized a list of ICMEs observed by different spacecraft/detectors at different locations to identify potential ICME events with multiple observations and investigate their evolution during propagation.

The layout of the article is as follows: Section 2 introduces the list of ICMEs and in situ observation data used in this study, methods for determining the multipoint observation of ICMEs, and methods for estimating the velocity and radius of ICMEs. Section 3 describes the evolution of some ICME parameters and the deflection of ICMEs during propagation. Our main results are summarized and discussed in Section 4.

2. Data and Methods

In this work, we used ICME lists and magnetic field and plasma data observed by the MESSENGER (MES), the VEX, the twin STEREO (including STEREO-A and STEREO-B), the Wind, the Juno, the Parker Solar Probe (PSP), the Mars Atmosphere and Volatile EvolutioN (MAVEN), the Solar Orbiter (SO), the BepiColombo (Bepi), and the Ulysses spacecraft/probes (Chi et al., 2016; Davies et al., 2021; Ebert et al., 2009; Good & Forsyth, 2016; Jian et al., 2018; Möstl et al., 2017, 2020; Winslow et al., 2015; Zhao et al., 2021). Detailed descriptions of the instruments on these spacecraft/probes can be found in the literature: for MES, see Anderson et al. (2007); for VEX, see Zhang et al. (2006); for twin STEREO, see Galvin et al. (2008) and Luhmann et al. (2008); for Wind, see Ogilvie et al. (1995) and Lepping et al. (1995); for Juno, see Connerney et al. (2017); for PSP, see Bale et al. (2016) and Kasper et al. (2016); for MAVEN, see Connerney et al. (2015) and Halekas et al. (2015); for SO, see Horbury et al. (2020) and Owen et al. (2020); for Bepi see Glassmeier et al. (2010) and Heyner et al. (2021), and for Ulysses see Wenzel et al. (1989). Based on the ICME lists compiled from observations by these spacecraft, we identified 33 ICME events with multipoint observations. The determination method is as follows: First, we use the typical propagation velocity of ICMEs to estimate the time of ICMEs from the previous observation point to the latter observation point. And we compare the estimated time with the ICME list of the latter observation point, selecting the most likely related ICME event based on the estimated arrival time. Then, on the basis of the observed data, we plotted a normalized magnetic field three-component comparison graph of these ICMEs in the Heliocentric Inertial (HCI) coordinate system, retaining ICME events with similar shapes in the normalized magnetic field three-component curve. Finally, we calculate the longitudinal differences in these ICMEs at different observation points, retaining ICMEs with longitudinal differences of less than 20°. Table 1 shows the identified multipoint observed ICME events. The first column is the event label, and the second column

is the name of the observer. The third and fourth columns are the start and end times of ICMEs, respectively. Based on the original event lists, we made slight adjustments to these time intervals according to the root mean square error of the normalized magnetic field three components at the two spacecraft, in order to refine the ICME boundaries and better support the subsequent analysis. The fifth, sixth, and seventh columns are the longitude, latitude, and radial distance (in the HCI coordinate system), respectively, at which the observer observes ICMEs. The eighth and ninth columns are the differences in longitude and radial distance between the pairwise observers, respectively. The tenth column presents the quality of the magnetic field structure of ICMEs ("bad" refers to the presence of interplanetary structure such as shock wave or current sheet in the ICME that cause drastic changes in the magnetic field, whereas 'good' refers to the opposite). The eleventh column indicates whether there is an observation of plasma data when ICMEs are observed ('yes' indicates that at least one observer has observed plasma data, whereas 'no' indicates the opposite). Figure 1 shows the time variation of the three-component of the normalized magnetic field for event Label 18. The graph shows that the normalized magnetic field three-component morphology observed by VEX (B_x/B_t, B_y/B_t, B_z/B_t) is very similar to the magnetic field three-component morphology observed by STEREO-A, with only slight differences in the magnitude of the values.

We removed multiple ICME (M-ICME) events from Table 1 according to the criteria of Shen et al. (2017) and eliminated events with a magnetic field structure 'bad' (which refers to the presence of structures such as shock waves or current sheets in the ICMEs ejecta), plasma data 'no', and a radial distance difference of less than 0.05 AU. We examine the remaining events and exclude the magnetosphere/magnetosheath data from the events. The region within the magnetosheath and magnetosphere can be identified by the crossings of bow shock, which are characterized by sudden changes in the strength of the magnetic field (Wang et al., 2018), as shown by the lavender-shadowed regions in Figure 2. We give the start and end times of the magnetosphere/magnetosheath regions in ICMEs in Table 2. Then, we use the velocity-modified cylindrical force-free flux rope model proposed by Wang et al. (2015) to fit the remaining ICMEs, preserving the handedness (H) consistent ICMEs in the event group, and we do not analyze the other ICMEs here. Finally, only 14 multipoint observation ICME events, which had also been present in some previous studies, were retained. By fitting, we can obtain several ICME parameters: the magnetic field strength (B_0) on the ICME axis, the elevation (θ) and azimuthal angles (ϕ) of the flux rope (θ ranges from $-90°$ to $90°$, and ϕ is defined counterclockwise from the positive x-direction toward the sun, ranging from $0°$ to $360°$); the closest distance (d) of the observed path from the axis of the flux rope; the handedness (H) of the flux rope; the axial magnetic flux (F_Z); the helicity (H_m); and the normalized root-mean-square error (χ_n) used to evaluate the goodness of fit.

Figure 3 shows the in situ data and fitting result of the ICME observed by the MES and Stereo-B in the event Label 8. From the figure, we can see that the fitted results of the three components of this ICME magnetic field are in good agreement with the observed data. Event Label 8 has been extensively studied (Amerstorfer et al., 2018; Good et al., 2018, 2019; Good & Forsyth, 2016; Vršnak et al., 2019) but only Vršnak et al. (2019) and Good et al. (2019) provided the fitting parameters. Table 3 presents the fitting results of this paper and theirs. The fitting models used by Good et al. (2019) and Wang et al. (2015) are both cylindrical force-free flux rope models (Lundquist solutions model (Burlaga, 1988; Lepping et al., 1990)), but the methods they used to find the best-fit are different. The method used by Wang et al. (2015) was non-linear least squares fitting (Markwardt, 2009), while Good et al. (2019) employed Minimum variance analysis (Goldstein, 1983) and Nelder-Mead simplex method. The fitting model used by Vršnak et al. (2019) is the force-free uniform-twist Gold–Hoyle configuration model (Gold & Hoyle, 1960; Wang, Zhuang, et al., 2016). From Table 3, we can find that (a) The axial magnetic field strength and radius obtained by fitting the three models are not significantly different, around 10%, and the power-law exponents of the axial magnetic field strength and radius with the radial distance are also not significantly different. (b) The θ and ϕ obtained by fitting at the MES are quite different, but the changing trends of θ and ϕ seem to be the same. With the propagation of ICME, $|\theta|$ has a decreasing trend, and ϕ has a tendency to lean toward the solar east. Overall, there are no systematic differences among these three models.

Because some spacecraft do not carry plasma detectors, some ICME in situ data are missing plasma data, so we cannot obtain the ICME propagation speed. Therefore, we use the average velocity method to estimate the propagation speed of ICMEs from missing plasma data. The formula we used to estimate the radius of ICMEs is $R = \frac{v\Delta t\sqrt{1-\cos^2\theta\cdot\cos^2\phi}}{2\sqrt{1-d^2}}$ (except for event Label 14 in Table 4, because in this Group event the radius of ICMEs are obtained directly by fitting) and where v is the propagation speed of the ICME, Δt is the duration of the ICME, and where θ, ϕ and d are the fitted elevation angle, azimuth angle and closest distance, respectively. This ICME radius

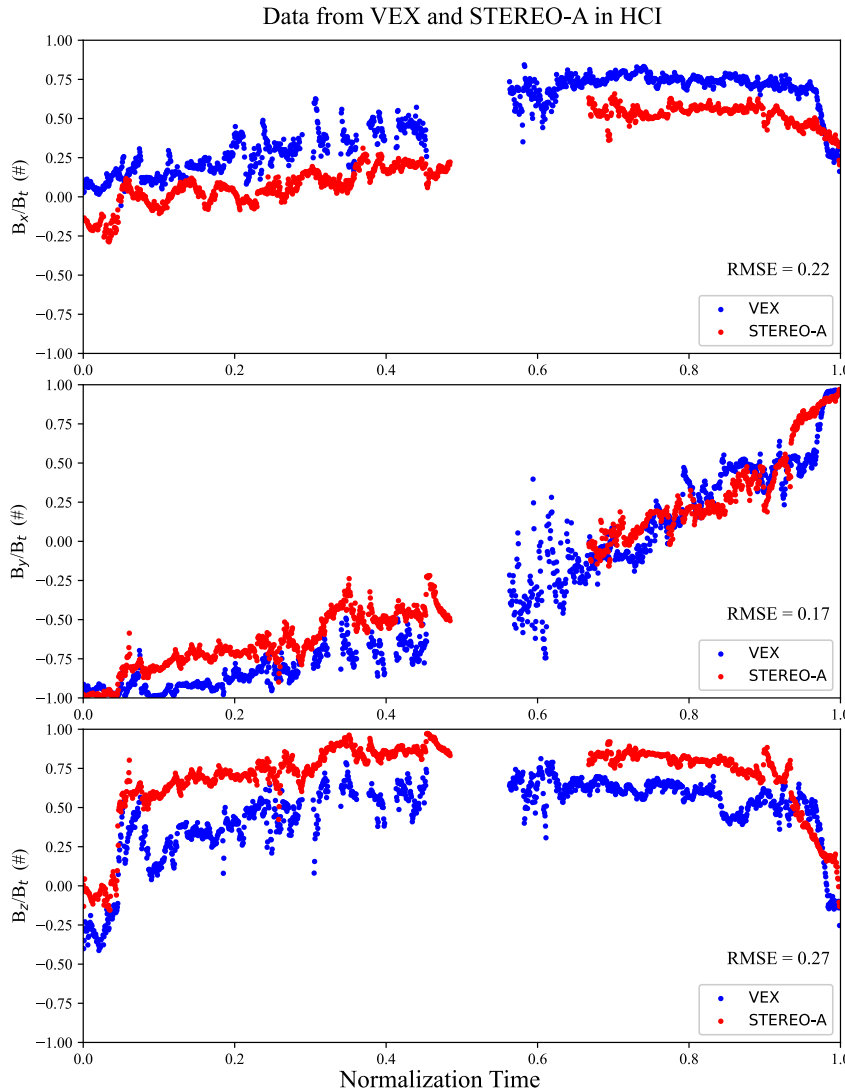

Figure 1. The normalized three-component variation map of the ICMEs magnetic field of event Label 18 observed by venus express (VEX) and STEREO-A. The data gaps in VEX are caused by the spacecraft entering the magnetosphere, and the data gap in STEREO-A is missing data. From top to bottom, the panels are normalized to the x, y and z components of the magnetic field in the HCI coordinate system. B_x/B_t indicates the ratio of the x component of the magnetic field to the total strength of the magnetic field. The same applies to B_y/B_t and B_z/B_t. The blue dots represent the magnetic field components of the interplanetary coronal mass ejection (ICME) as observed by VEX, and the red dots represent STEREO-A. The RMSE represents the root-mean-square error between them. "0" Represents the start time of the ICME, and "1" represents the end time of the ICME.

estimation formula was obtained from Vršnak et al. (2019). We find that this calculation formula is not suitable for estimating the radius of the ICME when θ approaches 0° and where ϕ approaches 180° or 360°). Therefore, we eliminate event groups where the fitting parameter θ is close to 0° and ϕ is close to 180° or 360°). Finally, we also calculate the axial magnetic flux Φ_z and helicity H_m by using the formulas for calculating the axial magnetic flux and helicity given by Wang et al. (2015).

3. Results and Analysis

Table 4 lists the fitting parameters for 14 sets of ICMEs, estimation results of the velocity and radius, and power exponent values (PE) of the power-law relationship between the average total magnetic field strength (B_t), axial magnetic field strength (B_0), radius (R), axial magnetic flux (Φ_z), helicity (H_m) and radial distance (D). The labels in the brackets in the first column of Table 4 correspond to the labels in Table 1. The eighth column (the closest

Table 1
The List of Multipoint Observation ICME Events

Label	Observer	Time begin	Time end	ϕ'	θ'	D	$\Delta\phi'$	ΔD	Structure	Plasma
1	Wind[a]	1998-03-04T14:37:30	1998-03-05T20:29:09	88.11	−7.31	0.98	6.21	4.42	bad	yes
	Ulysses[b]	1998-03-23T13:30:00	1998-03-28T18:00:00	81.90	−4.90	5.40				
2	Wind[a]	2007-05-21T22:24:00	2007-05-22T13:15:00	164.52	−1.91	1.00	2.72	0.06	bad	yes
	STB[c]	2007-05-22T04:20:00	2007-05-22T22:00:00	161.80	−2.60	1.06				
3	MES[d]	2007-05-24T22:45:07	2007-05-25T05:54:14	112.40	−1.60	0.67	1.31	0.05	good	no
	VEX[d]	2007-05-25T03:36:00	2007-05-25T09:44:00	113.71	−3.50	0.72				
4	VEX[d]	2008-12-29T20:45:36	2008-12-30T07:48:05	329.08	1.94	0.72	9.02	0.31	good	yes
	STB[c]	2008-12-31T04:00:00	2008-12-31T21:25:00	338.10	3.00	1.03				
5	VEX[d]	2009-06-02T18:38:53	2009-06-03T12:20:10	218.16	2.40	0.73	9.04	0.23	bad	yes
	STA[c]	2009-06-03T06:42:00	2009-06-04T22:40:00	227.20	5.50	0.96				
6	VEX[d]	2009-07-10T17:15:55	2009-07-11T06:02:29	278.26	3.81	0.73	9.66	0.23	good	yes
	STA[c]	2009-07-11T23:30:00	2009-07-12T19:20:00	268.60	7.30	0.96				
7	MES[d]	2009-08-28T01:22:05	2009-08-28T15:36:00	212.20	−2.20	0.56	3.60	0.52	bad	yes
	STB[c]	2009-08-30T16:20:00	2009-08-31T05:40:00	208.60	3.30	1.08				
8	MES[d]	2010-11-05T16:52:19	2010-11-06T13:07:41	246.60	−0.40	0.46	0.40	0.62	good	yes
	STB[c]	2010-11-08T02:46:00	2010-11-09T09:06:00	247.00	6.60	1.08				
9	VEX[d]	2011-03-19T04:53:04	2011-03-20T00:32:05	187.03	0.52	0.73	4.27	0.23	good	yes
	STA[c]	2011-03-19T23:34:00	2011-03-21T00:10:00	191.30	1.50	0.96				
10	VEX[d]	2011-03-22T17:28:02	2011-03-23T18:20:44	192.61	0.89	0.73	1.89	0.23	good	yes
	STA[c]	2011-03-23T06:55:00	2011-03-24T23:17:00	194.50	1.90	0.96				
11	VEX[d]	2011-04-05T16:25:37	2011-04-06T02:50:00	214.69	2.24	0.73	5.49	0.23	good	yes
	STA[c]	2011-04-06T09:40:00	2011-04-06T23:41:00	209.20	3.70	0.96				
12	VEX[d]	2011-04-20T06:51:50	2011-04-20T22:00:29	237.78	3.30	0.73	12.78	0.23	good	yes
	STA[c]	2011-04-21T07:12:00	2011-04-22T10:58:00	225.00	5.30	0.96				
13	MES[d]	2011-10-15T11:16:48	2011-10-16T06:23:02	161.70	−3.40	0.46	3.71	0.26	good	no
	VEX[d]	2011-10-16T06:57:36	2011-10-17T09:38:53	165.41	−0.90	0.73				
14	Wind[a]	2011-10-31T00:58:30	2011-11-01T17:19:00	321.47	4.59	0.98	2.98	0.30	bad	yes
	Juno[e]	2011-11-02T10:22:30	2011-11-04T08:19:30	324.45	4.16	1.28				
15	MES[d]	2011-11-05T01:03:12	2011-11-05T14:45:17	221.30	−1.80	0.44	4.30	0.65	good	yes
	STB[c]	2011-11-06T22:50:00	2011-11-08T18:00:00	225.60	5.00	1.09				
16	MES[d]	2011-12-31T02:23:58	2011-12-31T09:10:10	128.00	−2.80	0.42	4.40	0.54	good	yes
	STA[c]	2012-01-01T17:00:00	2012-01-02T04:00:00	132.40	−5.40	0.96				
17	STB[c]	2012-05-13T03:50:00	2012-05-14T03:00:00	38.70	−4.30	1.00	4.09	1.14	good	yes
	Juno[e]	2012-05-18T19:10:30	2012-05-20T15:40:37	42.79	−5.00	2.14				
18	VEX[d]	2013-01-08T15:54:32	2013-01-09T19:17:32	166.96	−0.82	0.73	4.96	0.24	good	yes
	STA[c]	2013-01-09T11:30:00	2013-01-10T17:00:00	162.00	−2.20	0.96				
19	Wind[a]	2013-04-14T16:39:00	2013-04-15T18:00:00	129.10	−5.59	0.99	1.06	0.62	good	yes
	Juno[e]	2013-04-17T01:21:30	2013-04-19T20:47:29	130.16	−5.60	1.61				
20	MES[f]	2013-05-01T08:51:54	2013-05-01T22:30:12	277.20	1.40	0.36	5.00	0.60	good	yes
	STA[c]	2013-05-03T05:50:00	2013-05-04T16:10:00	282.20	7.20	0.96				
21	MES[f]	2013-07-11T04:22:28	2013-07-11T22:53:30	215.80	−2.00	0.45	0.89	0.56	good	yes
	Wind[a]	2013-07-13T05:30:00	2013-07-14T23:33:00	214.91	4.13	1.01				
22	MES[f]	2013-09-13T04:50:17	2013-09-13T16:29:03	147.80	−3.30	0.45	8.80	0.59	good	yes
	STB[c]	2013-09-16T04:20:00	2013-09-17T00:25:00	139.00	−5.00	1.04				

Table 1
Continued

Label	Observer	Time begin	Time end	ϕ'	θ'	D	$\Delta\phi'$	ΔD	Structure	Plasma
23	Wind[a]	2013-12-01T13:30:00	2013-12-02T23:54:22	353.86	0.80	0.98	0.79	0.37	good	yes
	Juno[e]	2013-12-02T21:44:30	2013-12-04T19:18:29	354.65	4.30	1.35				
24	MAVEN[g]	2016-01-19T01:47:00	2016-01-22T01:58:00	106.54	−5.60	1.65	10.84	3.68	bad	yes
	Juno[e]	2016-02-09T11:08:11	2016-02-13T00:02:31	95.70	−5.35	5.33				
25	Wind[a]	2016-03-05T18:08:34	2016-03-06T17:10:10	89.47	−7.23	0.98	8.03	4.40	good	yes
	Juno[e]	2016-03-22T04:53:31	2016-03-23T19:42:52	97.50	−5.46	5.38				
26	SO[g]	2020-04-19T10:00:00	2020-04-20T07:05:00	129.96	−3.90	0.81	5.12	0.19	good	yes
	Wind[a]	2020-04-20T07:55:42	2020-04-21T06:25:42	135.08	−5.13	1.00	1.52	0.01		
27	Bepi[g]	2020-04-20T08:50:00	2020-04-21T07:50:00	133.56	−5.50	1.01	3.60	0.20		
	Bepi[g]	2020-05-29T15:27:00	2020-05-30T05:00:00	167.49	−2.73	0.98	5.60	0.03	good	yes
	Wind[g]	2020-05-30T04:18:00	2020-05-30T15:54:00	173.09	−0.88	1.01				
28	Bepi[g]	2021-05-25T00:27:00	2021-05-26T04:42:00	56.18	−3.24	0.79	16.11	0.16	bad	yes
	SO[g]	2021-05-27T20:14:00	2021-05-28T10:27:00	72.29	−0.98	0.95				
29	Bepi[g]	2021-07-01T01:14:00	2021-07-01T17:24:00	99.66	−3.80	0.83	3.77	0.08	good	no
	SO[g]	2021-07-01T11:12:00	2021-07-02T03:43:00	103.43	−1.75	0.91				
30	Bepi[g]	2021-07-25T22:10:00	2021-07-26T10:48:00	129.52	−2.95	0.78	0.26	0.02	good	no
	SO[g]	2021-07-26T01:38:00	2021-07-26T11:00:00	129.78	−2.02	0.81				
31	PSP[g]	2021-09-12T15:53:00	2021-09-13T07:39:00	236.02	3.23	0.72	1.77	0.24	good	yes
	STA[g]	2021-09-13T16:58:00	2021-09-14T12:22:00	234.25	6.02	0.96				
32	SO[g]	2021-10-30T22:19:00	2021-10-31T07:48:00	319.72	2.10	0.82	2.62	0.16	bad	yes
	Wind[g]	2021-10-31T09:34:00	2021-10-31T14:50:00	322.34	4.42	0.98				
33	SO[g]	2021-11-04T00:20:00	2021-11-04T19:38:00	324.85	2.00	0.85	1.34	0.14	good	yes
	Wind[a]	2021-11-04T07:00:00	2021-11-05T04:17:08	326.19	4.02	0.98				

Note. ϕ', θ' and D are the longitude, latitude and radial distance in the HCI coordinate system, respectively. $\Delta\phi'$, ΔD are the differences in longitude and radial distance between the two spacecraft, respectively. "Bad" refers to the presence of structures such as shock waves or current sheets in the ICMEs ejecta that cause drastic changes in the magnetic field, whereas "good" refers to the opposite. "Yes" means that the spacecraft has observed plasma data at this time, and 'no' means that it does not. D and ΔD are in units of AU, and θ', ϕ' and $\Delta\phi'$ are in units of degree. MES: MESSENGER; VEX: Venus Express; STA: STEREO-A; STB: STEREO-B; PSP: Parker Solar Probe; MAVEN: Mars Atmosphere and Volatile EvolutioN; SO: Solar Orbiter; Bepi: BepiColombo. [a]Events from Chi et al. (2016). [b]Events from Ebert et al. (2009). [c]Events from Jian et al. (2018). [d]Events from Good and Forsyth (2016). [e]Events from Davies et al. (2021). [f]Events from Winslow et al. (2015). [g]Events from Möstl et al. (2017, 2020).

distance d) and ninth column (normalized root-mean-square χ_n) of Table 4 can often be used to evaluate the goodness of fit (Lepping et al., 2006; Wang et al., 2015). The absolute values of d in Table 4 are all less than 0.95, and those of χ_n are less than 0.6, which indicates that these ICMEs are well fitted. According to Tables 1 and 4, the minimum longitude difference of the ICMEs involved in this study is 0.40°, and the maximum longitude difference is 9.02°. The radial distance ranges from 0.36 AU to 2.14 AU. The minimum radial distance difference is 0.14 AU, and the maximum radial distance difference is 1.14 AU.

3.1. Total Magnetic Field Strength and Axial Magnetic Field Strength

We studied the evolution of the average total magnetic field strength (B_t), axial magnetic field intensity (B_0) and radius (R) of ICMEs during interplanetary propagation. Figure 4a) shows the distribution of the average total magnetic field strength for each set of ICMEs as the radial distance changes in a double-logarithmic coordinate system. In Figures 4a, 4c and 4e, the colors indicate different ICME groups, while the dashed lines represent the corresponding trends within each group, consistent with the representation in Figures 6a and 6c. From Figure 4a, we can obtain $B_t(D)_a : B_t \propto D^{-1.68\pm0.17}$, with a Pearson correlation coefficient of cc $= -0.89$. This dependence indicates that the rate of decay of the average total magnetic field strength is slightly less than would be expected

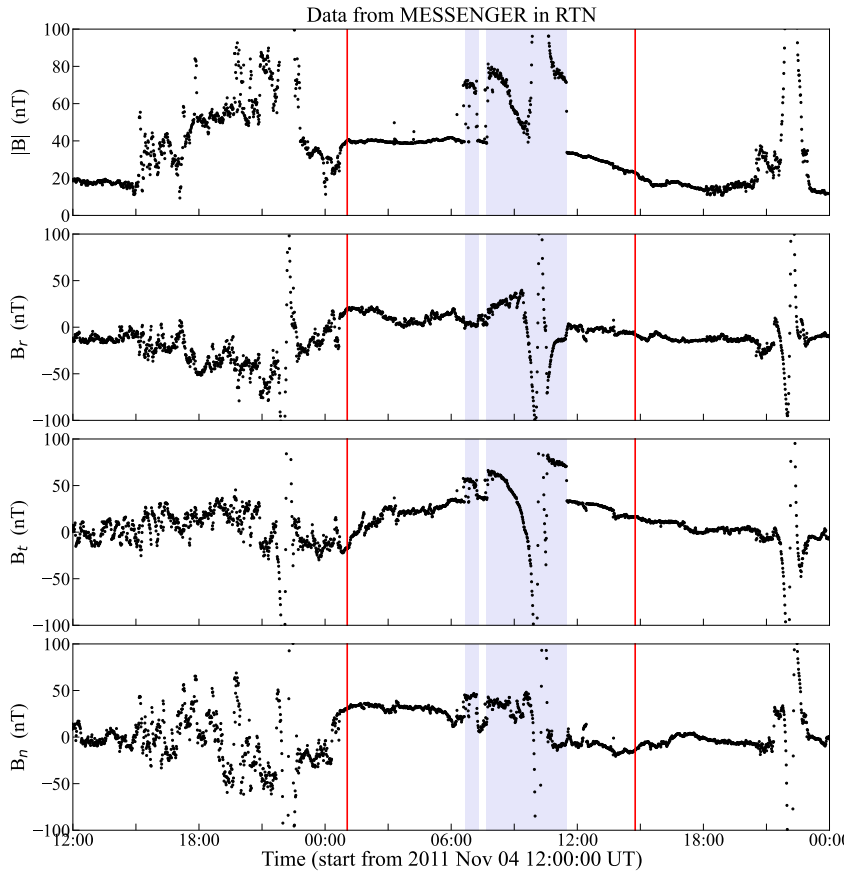

Figure 2. Magnetic field measured by MESSENGER. From top to bottom, the panels represent the total magnetic field strength $|B|$, the R component B_R, the T component B_T and the N component B_N of the magnetic field, respectively. The black dots indicate the magnetic field in situ data. The red vertical lines represent the start and end times of the interplanetary coronal mass ejection body. The lavender-shadowed regions indicate the magnetosheath and magnetosphere behind the planetary bow shock.

from isotropic self-similar expansion. Our result is slightly different from the conclusions ($B_t \propto D^{-1.52}$ and $B_t \propto D^{-1.40 \pm 0.08}$) of Liu et al. (2005) and Wang et al. (2005). In the study of Liu et al. (2005) and Wang et al. (2005), they analyzed 216 and 600 ICMEs respectively, all of which mainly occurred in Solar Cycles 21 and 23, with radial distance ranging from 0.3 to 5.4 AU. However, in this study, only 28 (14 groups) ICME events were involved, with radial distance ranging from $0.36 - 2.14$ AU, and the events were mainly occurred in Solar Cycle 24. The difference in the number of ICMEs, the difference in the range of radial distance and the difference in the space environment caused by the different degree of solar activity may be the cause of the difference in the power-law rate relationship between the average total magnetic field strength and the radial distance.

We also separately fit the power-laws of B_t and D for each group of ICMEs, and the fitted power-law exponents PE_{B_t} are shown in Table 4 and Figure 4b. From Figure 4b, we find that PE_{B_t} presents a relatively large scatter distribution (from -2.13 to -0.69), which is also present in the studies of Davies et al. (2022), Good et al. (2019), I. G. Richardson (2014), Salman et al. (2020) and Vršnak et al. (2019). This distribution indicates a significant difference in the radial dependence of the average total magnetic field intensity among each group of ICMEs. We calculate the mean and standard deviation of PE_{B_t}, and thus obtain a power-law relationship between B_t and D, $B_t(D)_b : B_t \propto D^{-1.48 \pm 0.44}$. Unsurprisingly, the results also show that the rate of decay of the average total magnetic field strength is slightly lower than would be expected from isotropic self-similar expansion. The power-law relationship between B_t and D obtained in this study is very close to $B_t(D) : B_t \propto D^{-1.46 \pm 0.53}$ obtained by Davies et al. (2022).

Table 2
Magnetosphere/Magnetosheath Regions in Some ICMEs

		ICME		Magnetosphere/Magnetosheath	
Label	Observer	time begin	time end	time begin	time end
1 (15)	MES[a]	2011-11-05T01:03:12	2011-11-05T14:45:17	2011-11-05T06:40:00	2011-11-05T07:18:00
				2011-11-05T07:40:00	2011-11-05T11:30:00
2 (18)	VEX[a]	2013-01-08T15:54:32	2013-01-09T19:17:32	2013-01-08T23:50:00	2013-01-09T00:13:00
				2013-01-09T00:47:00	2013-01-09T01:13:00
				2013-01-09T01:50:00	2013-01-09T02:13:00
				2013-01-09T02:50:00	2013-01-09T03:13:00
				2013-01-09T04:20:00	2013-01-09T07:20:00
3 (20)	MES[b]	2013-05-01T08:51:54	2013-05-01T22:30:12	2013-05-01T15:25:00	2013-05-01T16:50:00
4 (21)	MES[b]	2013-07-11T04:22:28	2013-07-11T22:53:30	2013-07-11T06:10:00	2013-07-11T10:20:00
				2013-07-11T11:25:00	2013-07-11T18:05:00
5 (22)	MES[b]	2013-09-13T04:50:17	2013-09-13T16:29:03	2013-09-13T05:20:00	2013-09-13T05:40:00
				2013-09-13T08:20:00	2013-09-13T11:50:00
				2013-09-13T12:20:00	2013-09-13T13:30:00

Note. The labels in parentheses in column 1 correspond to those in Table 1. [a]events from Good and Forsyth (2016). [b]events from Winslow et al. (2015).

Figure 4c shows the distribution of the axial magnetic field strength with the radial distance in a double logarithmic coordinate system. The colors and dashed lines in Figure 4c have the same meaning as those in Figure 4a. From Figure 4c, we can obtain the power-law relationship B_0 with D, $B_0(D)_a : B_0 \propto D^{-1.54 \pm 0.15}$, Pearson correlation coefficient cc $= -0.90$, which is similar to $B_t(D)_a$. $B_0(D)_a$ differs slightly from the conclusions of Good et al. (2019) ($PE = -1.76 \pm 0.04$, ranging from 0.32 − 1.1 AU), Farrugia et al. (2005) ($PE = -1.73$, ranging from 0.3 − 1 AU), and Leitner et al. (2007) ($PE = -1.64 \pm 0.40$, ranging from 0.3 − 1 AU), likely due to variations in the radial distance ranges analyzed in each study. Similarly, we separately fit B_0 and D for each group of ICMEs, and the fitted power exponents PE_{B_0} are shown in Figure 4d. From Figure 4d, we find that PE_{B_0} also exhibits a relatively large scatter distribution, ranging from −2.01 to −0.26, which is larger than the range of PE_{B_t}. Another power-law relationship between B_0 and D obtained by calculating the mean and standard deviation of PE_{B_0}, $B_0(D)_b : B_0 \propto D^{-1.36 \pm 0.51}$, is also similar to $B_t(D)_b$. $B_0(D)_b$ is basically consistent with another conclusion $B_0 \propto D^{-1.34 \pm 0.71}$ reached by Good et al. (2019). Both $B_0(D)_a$ and $B_0(D)_b$ indicate that the decay rate of the axial magnetic field strength is slightly slower than the expected isotropic self-similar expansion.

3.2. Flux Rope Radius

Figure 4e shows the distribution of the flux rope radius with the radial distance in a double logarithmic coordinate system. From Figure 4e, we can obtain the power-law relationship R with D, $R(D)_a : R \propto D^{0.84 \pm 0.22}$, and the Pearson correlation coefficient cc $= 0.62$. The $R(D)_a$ is consistent with the results of Vršnak et al. (2019) and Bothmer and Schwenn (1998). The power exponent PE_R obtained via power-law fitting alone is shown in Figure 4f. Figure 4f shows that PE_R still presents a relatively large scatter distribution, ranging from 0.2 (slow expansion) to 1.04 (self-similar expansion). There are 36% (5 groups) of events that meet the expectation of self-similar expansion (PE_R from 0.9 − 1.1). Another power ratio relation between R and D is obtained by PE_R, $R(D)_b : R \propto D^{0.68 \pm 0.26}$. These dependencies indicate that the expansion rate of the radius is in line with the expected self-similarity expansion, but slightly slower.

We found that the radius expansion rate distribution of ICMEs is very dispersed. Here, we have attempted to try to explain this phenomenon. We divided 14 multipoint observation events into 4 groups according to the radial distance of the ICME event group, namely Group 1 (including Labels 2, 5, 8, 9, and 10, from ∼0.4 AU to ∼1 AU), Group 2 (Labels 1, 3, 4, 7, and 13, from ∼0.7 AU to ∼1 AU), Group 3 (Labels 12 and 14, from ∼0.8 AU to ∼1 AU), and Group 4 (Labels 6 and 11, events without the same start and end positions). Events in Group 4 were not included in the analysis. The maximum of the total magnetic field strength ($B_{\max}$) and the leading edge velocity

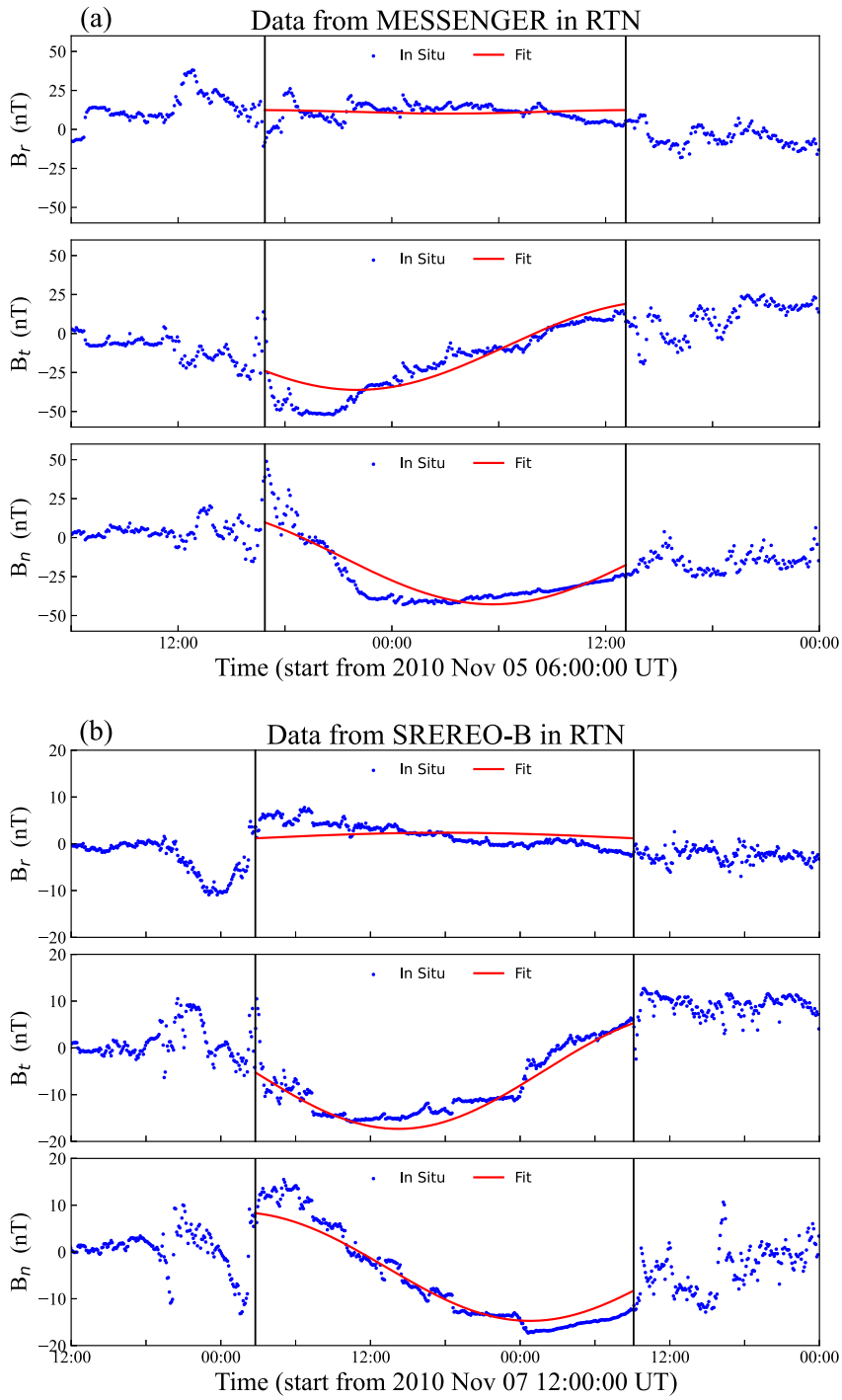

Figure 3. Comparison of in situ data and fitting result of interplanetary coronal mass ejection (ICME) observed by the MES and Stereo-B in event Label 8. Subfigure (a) shows the observational data and the fitting results of ICME at MESSENGER spacecraft, and subfigure (b) is at the Stereo-B spacecraft. The blue dots represent in situ observation data. The red lines represent the data obtained by fitting the flux rope model. The black vertical lines represent the start and end times of the ICME body.

Table 3
A Comparison of the Fitting Results of Different Fitting Models for Event Label 8

	MES						STB						PE_{B_t}	PE_R
Model	B_0	θ	ϕ	H	R	χ_n^2	B_0	θ	ϕ	H	R	χ_n^2		
This paper	55.4	−51.8	54.1	1	0.1175	0.096	19.09	−32.5	88.8	1	0.1531	0.084	−1.25	0.31
Vršnak et al. (2019)	49.8	−60.1	88.5	1	0.104	0.058	20.3	−32.2	82.8	1	0.145	0.063	−1.08	0.4
Good et al. (2019)	54.6	−38.8	142.8	1	/	0.07	19.9	−33.4	92.4	1	/	0.03	−1.19	/
Maximum deviation	10%	21.3	88.7	/	11%	/	6%	−0.9	3.6	/	5%	/	/	/

Note. The fitting model used in this paper was proposed by Wang et al. (2015). In the Vršnak et al. (2019), the parameter χ_n^2 is from the E_{rms} parameter. In the Good et al. (2019), the parameter ϕ is in the Spacecraft Equatorial (SCEQ) coordinate. The table gives the converted ϕ values.

(V_{ICME}) of each ICME and the magnetic field strength (B_{SW}) and velocity (V_{SW}) of the background solar wind were subsequently calculated, as shown in Table 5.

We also calculated the average PE_R of Group 1 and Group 2 (PE_{G1} and PE_{G2}), which excludes ICME events propagating in high-speed solar wind $(V_{SW} > V_{ICME})$ (Labels 1 and 13). Not surprisingly, we find that $PE_{G1} = 0.66 > PE_{G2} = 0.42$. This indicates that the expansion rate of the ICME propagating from ∼0.4 AU to ∼0.7 AU tends to be greater than the expansion rate propagating from ∼0.7 AU to ∼1.0 AU. Figure 5a shows the variation in the magnetic pressure differential with the radial distance at the initial positions in Group 1 and Group 2. The magnetic pressure difference decreases with increasing radial distance, which may be the reason for the larger expansion rate of the ICME as it propagates from ∼0.4 AU to ∼0.7 AU.

Figure 5b shows the distribution of the magnetic pressure difference (ΔP_B) between the ICME and the background solar wind at the initial position for each multipoint observed event in Groups 1, 2, and 3 with respect to the expansion rate of the ICME radius. We found that in Group 1, the expansion rate of the ICME increased with increasing magnetic pressure difference (positive correlation), whereas in Groups 2 and 3, the expansion rate of the ICME decreased with the increasing magnetic pressure difference (negative correlation). This indicates that the ICME propagates from approximately 0.4 AU to approximately 0.7 AU, and its radius expansion rate is usually related to the initial magnetic pressure difference, whereas other factors affect its expansion rate from approximately 0.7 AU to approximately 1 AU. This conclusion is similar to that of Lugaz et al. (2020).

Figure 5c shows the distribution of the velocity difference (ΔV) between the ICME and the background solar wind vs. the ICME expansion rate. We find that (a) in Group 2, the ICME propagating in high-speed solar wind $(\Delta V < 0)$ tends to expand faster than the ICME propagating in low-speed solar wind $(\Delta V > 0)$; (b) in both Group 2 and Group 3, the expansion rates of ICME decrease with increasing ΔV. According to the drag-based model proposed by Vršnak et al. (2013), the drag force received during ICME propagation is often proportional to the square of the velocity difference between the ICME and background solar wind. The larger the velocity difference is, the greater the drag force on the ICME, which may make it more difficult for the ICME to expand or even change the shape of the ICME cross-section.

In summary, the magnetic pressure difference and the velocity difference between the ICME and the background solar wind are two factors that affect the expansion rate of the ICME. This view is similar to that of Lugaz et al. (2020) and Démoulin and Dasso (2009). The dominant factors are different in different locations. At ∼0.4 − ∼0.7AU, the ICME expansion rate is affected mainly by the magnetic pressure difference. At ∼0.7 − ∼1.0 AU, the ICME expansion rate is influenced mainly by the velocity difference.

3.3. Axial Magnetic Flux and Helicity

Figure 6a shows the evolution of the axial magnetic flux and the power-law relationship between Φ_z and D, $\Phi_z(D)_a : \Phi_z \propto D^{0.14 \pm 0.52}$. The Pearson correlation coefficient of this power-law relationship is only cc = 0.05. Given the large uncertainty in the power-law exponent and the very low correlation coefficient and the fact that the start and end times of ICMEs chosen at one location may not exactly match those chosen at another location, the axial magnetic flux can therefore be considered constant. The PE_{Φ_z} of each group of ICMEs obtained via power-law

Table 4
ICMEs Parameters and Power Law Relationship of Parameters and Radial Distance

Label	Observer	B_t	B_0	θ	ϕ	H	d	χ_n	v	R	Φ_z	H_m	PE_{B_t}	PE_{B_0}	PE_R	PE_{Φ_z}	PE_{H_m}
1[a,b] (4)	VEX[c]	10.34	14.16	−12.7	319.3	−1	0.72	0.50	359	0.0466	9.22 E+19	1.30 E+41	−0.88	−0.76	1.02	1.29	2.55
	STB[d]	7.56	10.83	−3.4	329.8	−1	0.69	0.37	454	0.0669	1.45 E+20	3.22 E+41					
2[a,e] (8)	MES[c]	44.32	55.40	−51.8	54.1	1	−0.46	0.31	457	0.1175	2.29 E+21	2.04 E+43	−1.19	−1.25	0.31	−0.63	−0.58
	STB[d]	16.19	19.09	−32.5	88.8	1	−0.12	0.29	415	0.1531	1.34 E+21	1.25 E+43					
3[a,b] (9)	VEX[c]	16.58	16.82	−16.7	317.9	−1	0.60	0.58	542	0.1130	6.43 E+20	2.63 E+42	−1.96	−1.54	0.72	−0.10	0.08
	STA[d]	9.61	10.94	2.0	231.9	−1	−0.55	0.53	492	0.1382	6.26 E+20	2.69 E+42					
4[a,b] (11)	VEX[c]	17.08	25.57	15.6	36.7	1	−0.79	0.41	592	0.0768	4.52 E+20	1.91 E+42	−1.42	−1.60	0.35	−0.90	−1.15
	STA[d]	11.53	16.43	−0.5	40.7	1	−0.73	0.34	522	0.0846	3.52 E+20	1.39 E+42					
5[a,b] (15)	MES[c]	36.32	49.80	11.2	209.0	−1	−0.53	0.34	557	0.0556	4.62 E+20	1.67 E+42	−1.71	−1.75	0.57	−0.60	−0.78
	STB[d]	7.64	10.11	2.1	347.4	−1	0.65	0.35	619	0.0938	2.67 E+20	8.16 E+41					
6[f] (17)	STB[d]	10.83	17.60	6.1	222.7	−1	−0.93	0.38	354	0.1848	1.80 E+21	1.74 E+43	−1.45	−1.50	0.92	0.35	0.77
	Juno[g]	3.59	5.63	7.2	221.2	−1	−0.94	0.47	344	0.3728	2.34 E+21	3.12 E+43					
7[a,e,b] (18)	VEX[c]	18.63	22.98	70.6	286.5	1	0.49	0.34	493	0.1859	2.38 E+21	2.19 E+43	−0.69	−0.26	0.20	0.13	1.07
	STA[d]	15.34	21.36	64.2	200.8	1	0.56	0.28	500	0.1965	2.47 E+21	2.95 E+43					
8[b] (20)	MES[h]	101.61	98.93	−0.3	304.8	−1	−0.18	0.52	559	0.0768	1.75 E+21	1.43 E+43	−1.98	−2.01	0.91	−0.19	−0.29
	STA[d]	14.82	13.98	27.0	311.0	−1	−0.16	0.57	546	0.1860	1.45 E+21	1.07 E+43					
9[e] (21)	MES[h]	37.10	48.16	−6.0	253.6	−1	−0.33	0.35	477	0.1085	1.70 E+21	1.18 E+43	−1.37	−1.57	0.95	0.32	0.70
	Wind[i]	12.31	13.57	−27.6	280.4	−1	−0.06	0.36	463	0.2326	2.20 E+21	2.07 E+43					
10[b] (22)	MES[h]	32.95	32.17	6.7	71.1	1	−0.33	0.58	365	0.0515	2.56 E+20	5.62 E+41	−2.13	−1.83	0.58	−0.67	−0.92
	STB[d]	5.46	6.88	27.1	101.0	1	−0.42	0.33	319	0.0838	1.45 E+20	2.58 E+41					
11[f] (23)	Wind[i]	8.74	12.91	−35.1	202.6	−1	0.77	0.43	509	0.2178	1.84 E+21	1.49 E+43	−1.55	−1.65	0.59	−0.48	−0.54
	Juno[g]	5.29	7.57	−33.2	189.2	−1	0.85	0.55	450	0.2633	1.57 E+21	1.25 E+43					
12[j,k] (26)	SO[l]	18.74	21.44	9.9	86.6	−1	−0.24	0.41	333	0.0873	4.90 E+20	2.19 E+42	−1.24	−1.12	0.80	0.47	1.14
	Wind[i]	14.45	16.95	22.5	83.5	−1	−0.25	0.37	369	0.1031	5.40 E+20	2.79 E+42					
13[k] (31)	PSP[l]	11.24	14.91	36.4	76.0	−1	0.56	0.33	368	0.0828	3.06 E+20	8.08 E+41	−2.10	−1.78	1.04	0.29	0.55
	STA[l]	6.20	9.02	48.8	92.5	−1	0.67	0.29	353	0.1110	3.33 E+20	9.45 E+41					
14[k] (33)	SO[l]	18.38	20.47	−5.1	180.2	1	−0.71	0.32	–	0.0302	5.60 E+19	8.68 E+40	−1.04	−0.44	0.63	0.82	2.01
	Wind[i]	15.72	19.16	−2.6	182.3	1	−0.63	0.30	–	0.0332	6.33 E+19	1.17 E+41					
ave	–	–	–	–	–	–	–	–	–	–	–	–	−1.48	−1.36	0.68	0.01	0.33
std	–	–	–	–	–	–	–	–	–	–	–	–	0.44	0.51	0.26	0.61	1.08

Note. B_t is the average value of the total ICMEs' magnetic field strength calculated from the observed data. B_0, θ, ϕ, H, d, and χ_n are the axial magnetic field strength, elevation angle, azimuth angle, handedness, closest distance and normalized root-mean-square error of the fitted flux rope, respectively. v is the speed of the ICMEs derived from observations or estimates. R is the radius of the ICME flux rope. Φ_z and H_m are the axial magnetic flux and helicity of the ICME flux rope, respectively. PE_{B_t}, PE_{B_0}, PE_R, PE_{Φ_z} and PE_{H_m} are the power exponent values of the power law relationship between the total magnetic field strength, axial magnetic field strength, radius, axial magnetic flux and helicity and radial distance of ICMEs, respectively. "Ave" and "std" represent the average values and standard deviations of the power exponent, respectively. B_t and B_0 are in units of nT, θ and ϕ in units of degree, d in units of R, v in units of km · s^{-1}, R in units of AU, Φ_z in units of MX, and H_m in units of MX^2. The labels in parentheses in column 1 correspond to those in Table 1. Event Label 33: Due to the presence of plasma observation data from both observers, the radius of the flux rope can be directly obtained through fitting. [a]Good et al. (2019). [b]Salman et al. (2020). [c]events from Good and Forsyth (2016). [d]events from Jian et al. (2018). [e]Vršnak et al. (2019). [f]Davies et al. (2022). [g]events from Davies et al. (2021). [h]events from Winslow et al. (2015). [i]events from Chi et al. (2016). [j]Möstl et al. (2022). [k]the LineupCAT (https://helioforecast.space/lineups). [l]events from Möstl et al. (2017, 2020) and the ICMECAT (https://helioforecast.space/icmecat).

fitting is shown in Figure 6b, and another power-law relationship between Φ_z and D is obtained by using its average value and standard deviation, $\Phi_z(D)_b : \Phi_z \propto D^{0.01 \pm 0.61}$, which is compatible with $\Phi_z(D) = \text{constant}$.

We also investigated the evolution of the flux rope helicity during interplanetary propagation, as shown in Figure 6c. From Figures 6c and 6d, we can obtain two kinds of dependences between H_m and D, $H_m(D)_a : H_m \propto D^{0.43 \pm 0.84}$, with the Pearson correlation coefficient cc = 0.11 and $H_m(D)_b : H_m \propto D^{0.33 \pm 1.08}$. The

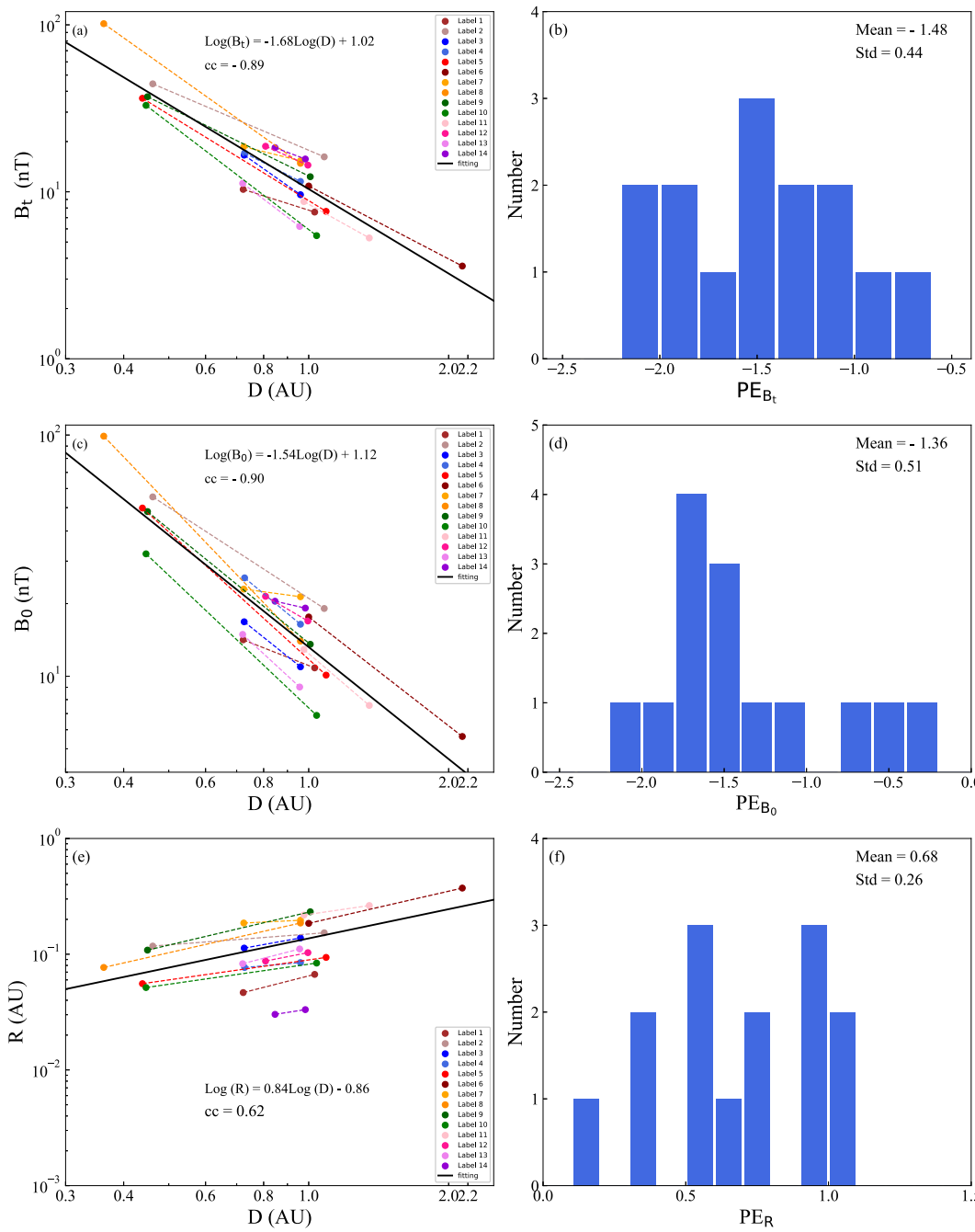

Figure 4. Evolution of the total magnetic field strength, axial magnetic field strength and radius of ICMEs. Panels (a, c, and e) show the power-law relationship of the total magnetic field strength, axial magnetic field strength, and radius with radial distance of all ICMEs, respectively (except for the Label 14 in Panels (c, e)). Each color represents a set of ICMEs. Dotted lines of different colors connect the same set of ICMEs the data points. The black dashed line represents the power-law relationship obtained by fitting all data points. "cc" is the correlation coefficient of the power law relationship. Panels (b, d and f) show the power-law exponential distribution of the total magnetic field strength, axial magnetic field strength, and radius with radial distance of each group of ICMEs, respectively. "Mean" and "Std" represent the mean and standard deviation of the power-law exponents.

Table 5
Classification and Parameters of ICME

Group	Label	D	PE_R	B_{max}	B_{SW}	ΔP_B	V_{ICME}	V_{SW}	ΔV
G1	2	0.46	0.31	54.88	12.75	0.1134	–	–	–
		1.08		17.65	2.46	0.0122	414.80	294.04	120.76
	5	0.44	0.57	71.53	17.35	0.1916	–	–	–
		1.09		10.06	4.47	0.0032	618.67	469.18	149.49
	8	0.36	0.91	162.65	34.67	1.0047	–	–	–
		0.96		21.94	3.81	0.0186	545.83	452.25	93.58
	9	0.45	0.95	75.11	22.13	0.2050	–	–	–
		1.01		16.43	5.09	0.0097	463.08	374.93	88.15
	10	0.45	0.58	73.32	29.71	0.1788	–	–	–
		1.04		6.29	5.53	0.0004	318.50	311.97	6.53
G2	1	0.72	1.02	20.97	7.52	0.0152	–	–	–
		1.03		8.98	5.78	0.0019	454.23	478.62	−24.39
	3	0.73	0.72	35.00	10.30	0.0445	–	–	–
		0.96		12.88	5.00	0.0056	492.23	401.49	90.74
	4	0.73	0.35	19.68	6.26	0.0139	–	–	–
		0.96		14.00	6.57	0.0061	522.27	394.12	128.15
	7	0.73	0.20	39.20	9.07	0.0579	–	–	–
		0.96		18.36	5.72	0.0121	500.10	357.55	142.55
	13	0.72	1.04	13.94	7.91	0.0052	–	–	–
		0.96		7.52	4.60	0.0014	353.10	387.00	−33.89
G3	12	0.81	0.80	21.20	3.86	0.0173	–	–	–
		1.00		16.29	2.44	0.0103	369.33	295.30	74.03
	14	0.85	0.63	24.65	7.59	0.0219	–	–	–
		0.98		23.64	2.81	0.0219	700.28	495.95	204.33

Note. B_{max}, V_{ICME}, B_{SW}, V_{SW}, ΔP_B and ΔV are the maximum ICME total magnetic field strength and leading edge velocity, the background solar wind magnetic field strength and velocity, and the magnetic pressure difference and velocity difference, respectively. The units of B_{max} and B_{SW} are nT. V_{ICME}, V_{SW} and ΔV are measured in km/s. The unit of ΔP_B is $\times 10^{-8}$ Pa. The quality of the magnetic field data in Label eight is not very good, and there may be a part of the magnetic field data in Mercury's magnetosphere.

dependence between H_m and D is similar to that between Φ_z and D, both of which have large uncertainties and very low correlation coefficients. Therefore, helicity can also be considered a constant.

3.4. Flux Rope Axis Orientation

ICMEs may interact with other ICMEs or interplanetary structures during interplanetary propagation, causing deflection of ICMEs (Gopalswamy et al., 2001; Liu et al., 2019; Lugaz et al., 2012; Shen et al., 2012; Wang et al., 2004, 2014). In this work, we studied how the flux rope axis orientation changes in the propagation process by fitting the elevation and azimuthal angles (θ and ϕ) obtained. Figure 7a shows the variation in elevation angle for each group of ICME. We find that in 57% (8/14) of cases the absolute value of θ decreases with the propagation of the ICME. If the cases that θ at the inner spacecraft is close to zero are removed, θ of 7/9 of the event are decreasing. This phenomenon indicates that with the propagation of ICME, the flux rope axis tends to approach horizontal. This result is consistent with the conclusion of Good et al. (2019). Figure 7b shows the distribution of azimuthal angle with radial distance. In this panel, there is a weak indication that the flux rope axis has a tendency toward the solar east ($\phi = 90°$) or the solar west ($\phi = 270°$), indicating a general east-west alignment. The changes in the elevation and azimuthal angles ($|\Delta\theta|$, $|\Delta\phi|$) of the same group of ICMEs under different radial distances are shown in Figure 7c–7e. When $|\Delta\theta| \geq 10°$ or $|\Delta\phi| \geq 20°$, we considered that the direction of the flux

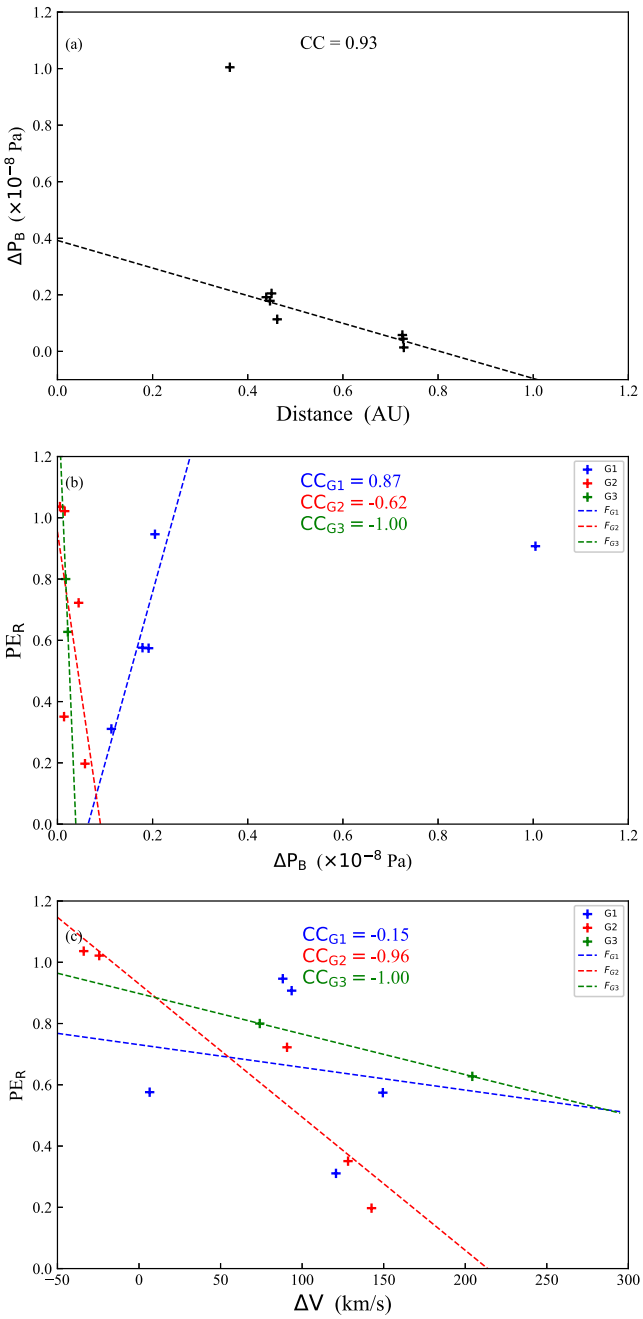

Figure 5. Correlation between ICMEs parameters. (a) Relationship between magnetic pressure difference between the interplanetary coronal mass ejection (ICME) and background solar wind and radial distance. (b) Distribution of the magnetic pressure difference between the ICME and the background solar wind and the expansion rate of the ICME radius. (c) The correlation between the ICME expansion rate and the velocity difference between the ICME and background solar wind. The blue fit results in panel (b) are obtained by removing Label 8.

rope axis has changed. From these three panels, we found that $|\Delta\theta|$ and $|\Delta\phi|$ generally have progressively decreasing distribution. 71% (10/14) of the events had a change in the direction of the flux rope axis (elevation or azimuthal angle changes), indicating that the propagation direction of part of ICMEs would change or the local flux rope structure would distort during interplanetary propagation.

4. Discussion and Conclusion

In this study, we established 33 ICME events with possible multipoint observations on the basis of interplanetary data and ICME lists observed by the MESSENGER, the VEX, the twin STEREO (including STEREO-A and STEREO-B), the Wind, the Juno, the Parker Solar Probe, the Mars Atmosphere and Volatile EvolutioN, the Solar Orbiter, the Bepi Colombo, and the Ulysses spacecraft or probes. The results are shown in Table 1. We have fitted the ICMEs of 14 groups of events that satisfied the conditions, which have also appeared in some previous studies, and the fitting results are shown in Table 4. On the basis of the fitted parameters and in situ observation data, we studied the power-law relationships between the average total magnetic field intensity, axial magnetic field intensity, radius, axial magnetic flux and helicity of ICMEs and the radial distance, and investigated the deflection during the interplanetary propagation of ICMEs. The main findings are as follows:

1. Through power-law fitting of all the data, we found power-law relationships between the average total magnetic field strength, axial magnetic field strength, and flux rope radius of ICMEs and the radial distance $B_t(D)_a : B_t \propto D^{-1.68\pm0.17}$, $B_0(D)_a : B_0 \propto D^{-1.54\pm0.15}$ and $R(D)_a$: $R \propto D^{0.84\pm0.22}$. The $PE_{B_{t,a}} = -1.68 \pm 0.17$ is slightly smaller than the $PE_{B_t} = -1.52$ obtained by Wang et al. (2005) and the $PE_{B_t} = 1.40 \pm 0.08$ obtained by Liu et al. (2005). This may be due to differences in the number of ICMEs analyzed, the range of radial distance, and the space environment. The $PE_{B_{0,a}} = -1.54 \pm 0.15$ is slightly larger than the conclusions of Good et al. (2019) ($PE = -1.76 \pm 0.04$), Farrugia et al. (2005) ($PE = -1.73$), and Leitner et al. (2007) ($PE = -1.64 \pm 0.40$), probably due to the larger maximum radial distance. The $PE_{R,a} = 0.84 \pm 0.22$ is basically consistent with the results of Vršnak et al. (2019) ($PE = 0.84 \pm 0.29$) and Bothmer and Schwenn (1998) ($PE = 0.78 \pm 0.10$).
2. By calculating the average and standard deviation of the power exponents of each group of events, other dependency relationships $B_t(D)_b : B_t \propto D^{-1.48\pm0.44}$, $B_0(D)_b : B_0 \propto D^{-1.36\pm0.51}$ and $R(D)_b : R \propto D^{0.68\pm0.26}$, are obtained. Only 36% of the event group is basically the expansion of the self-similar. The $PE_{B_{t,b}} = -1.48 \pm 0.44$ is basically consistent with the $PE = -1.46 \pm 0.53$ obtained by Davies et al. (2022). The $PE_{B_{0,b}} = -1.36 \pm 0.51$ is basically consistent with another conclusion $PE = -1.34 \pm 0.71$ reached by Good et al. (2019). However, the $PE_{R,b} = 0.68 \pm 0.26$ is different from the $PE = 0.38 \pm 1.08$ obtained by Vršnak et al. (2019). This may be because the study of Vršnak et al. (2019) includes a number of events in which the ICME radius decreases.
3. Similarly, the power-law relationships between axial magnetic flux and helicity and radial distance are obtained by all data fitting: $\Phi_z(D)_a : \Phi_z \propto D^{0.14\pm0.52}$ and $H_m(D)_a : H_m \propto D^{0.43\pm0.84}$. Obtain another power-law relationship between axial magnetic flux and helicity and radial distance through the mean and standard deviation: $\Phi_z(D)_b : \Phi_z \propto D^{0.01\pm0.61}$ and $H_m(D)_b : H_m \propto D^{0.33\pm1.08}$. These dependencies indicate that the axial magnetic

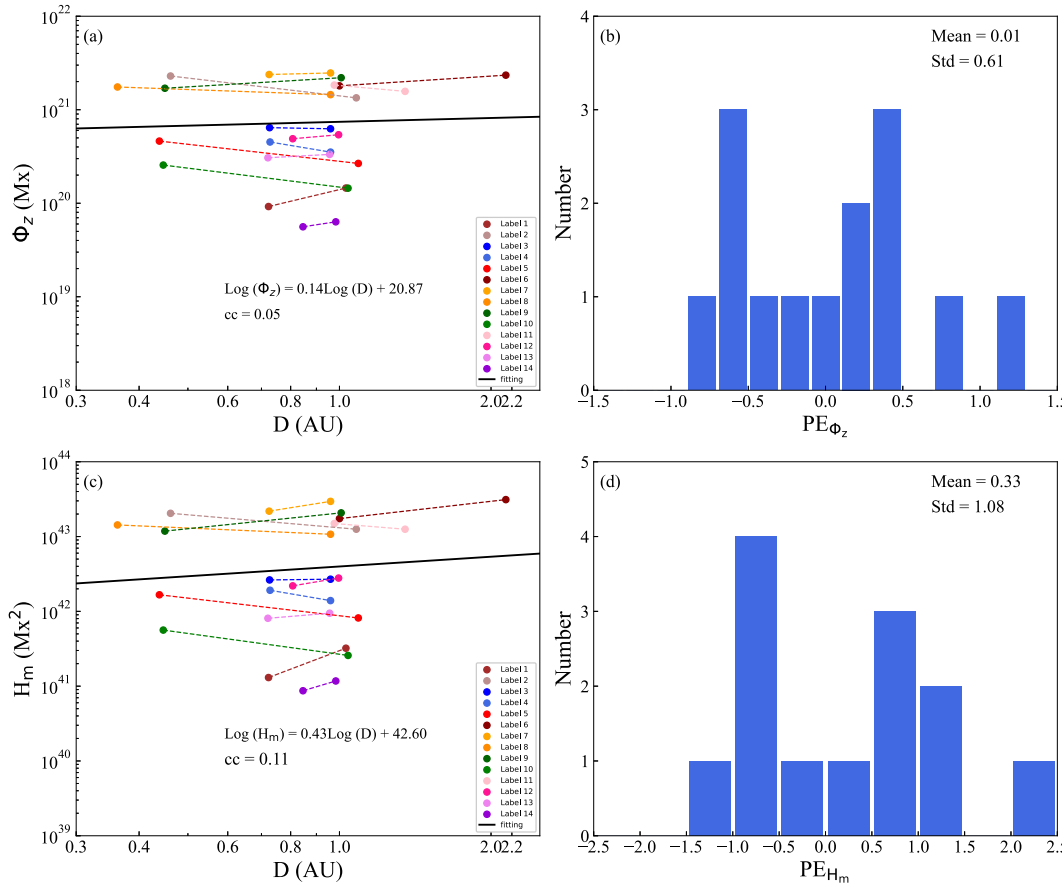

Figure 6. Evolution of the axial magnetic flux and helicity of ICMEs. Panels (a, c) show the power-law relationship of the axial magnetic flux and helicity with radial distance of all ICMEs, respectively (except for the Label 14). Each color represents a set of ICMEs. Dotted lines of different colors connect the same set of ICMEs data points. The black dashed line represents the power law relationship obtained by fitting all the data points. 'cc' is the correlation coefficient of the power-law relationship. Panels (b, d) show the power-law exponential distribution of the axial magnetic flux and helicity with radial distance of each group of ICMEs, respectively. "Mean" and "Std" represent the mean and standard deviation of the power exponents.

flux and helicity can be considered constant during ICMEs propagation, considering the large uncertainty of the power exponent and the very low correlation coefficient and that the start and end times of ICMEs are not exactly matched at different locations. These are consistent with the conclusion of Vršnak et al. (2019).

4. We find that the flux rope axis tends to be horizontal and solar west-east or east-west. We also find that the majority (71%) of the flux rope axis direction changes during interplanetary propagation, mainly due to changes in elevation angle. The conclusion is basically consistent with the conclusions of Good et al. (2019) and Davies et al. (2022).

Overall, the expansion rate of the flux rope radius is similar to the self-similar expansion expectation. However, the expansion rates of most events vary significantly, from slow expansion to self-similar expansion. We think this is caused by the magnetic pressure difference and velocity difference between ICMEs and the background solar wind. Around 0.4–0.7 AU, the magnetic pressure difference may be the dominant factor in the expansion rate of the ICME radius. The greater the magnetic pressure difference, the greater the expansion rate. At this stage, the ICME may expand faster than expected by self-similar expansion due to excessive magnetic pressure difference. With the propagation of ICME, the radial distance increases, the magnetic pressure difference decrease rapidly. The influence of magnetic pressure difference on radius expansion rate is gradually weakened, and the influence of velocity difference is gradually obvious. Near the $0.7 - 1$ AU, the dominant factor affecting ICME expansion becomes velocity difference. The expansion rate of an ICME propagating in a fast solar wind is

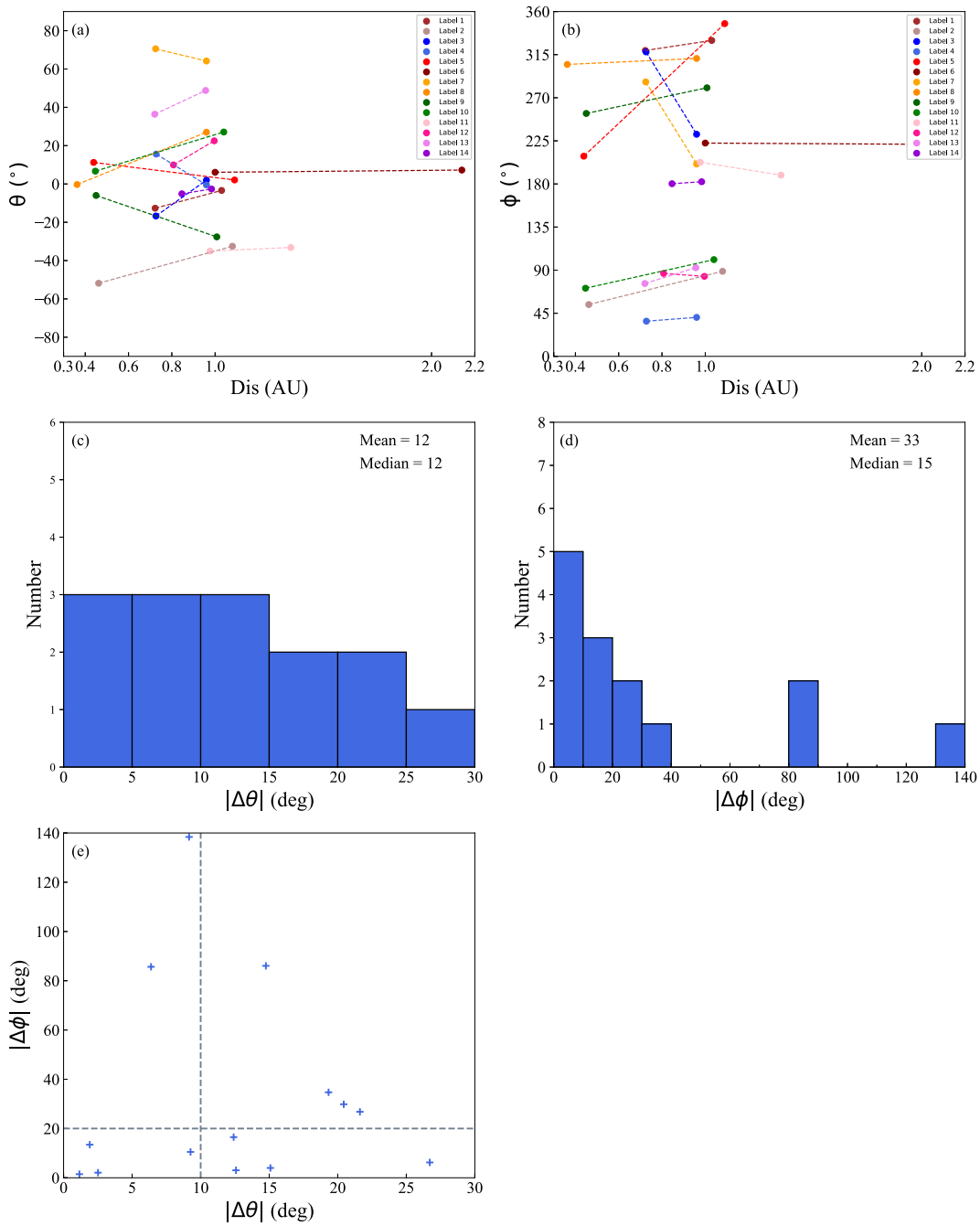

Figure 7. The deflection distributions of the elevation and azimuth angles of ICMEs. (a) The distribution of elevation angle (θ) with radial distance. (b) The azimuthal angel (ϕ) distribution with radial distance. Each color represents a set of ICMEs. Dotted lines of different colors connect the same set of ICMEs the data points. (c) Elevation deflection of ICMEs. $\Delta\theta$ is the change in the elevation angle of ICMEs during propagation. (d) Azimuth deflection of ICMEs. $\Delta\phi$ is the change in thr azimuth angle of ICMEs during propagation. (e) The simultaneous distribution of the elevation and azimuth deflection of ICMEs. The two dashed lines in panel (e) represent $|\Delta\theta| = 10°$ and $|\Delta\phi| = 20°$, respectively. 'Mean' and 'Median' in panels (c, d) represent the mean and median of the elevation angle or azimuth angle.

generally larger than that of an ICME propagating in a slow solar wind. In the slow (fast) solar wind, the larger the velocity difference, the smaller (larger) the expansion rate.

The decay rate of the magnetic field is not consistent with the expansion rate of the radius. A possible explanation is that ICMEs undergo magnetic reconnection with the magnetic field of the ambient solar wind during

propagation. Magnetic reconnection will strip the magnetic field outside the ICMEs, resulting in a decrease in the radius of the ICMEs and a decrease in magnetic flux (Wang et al., 2018). Another explanation is the 'pancaking' effect (Crooker & Intriligator, 1996; Manchester et al., 2004; Riley & Crooker, 2004; Riley et al., 2003; Russell & Mulligan, 2002). It means that due to the influence of slow solar wind, the cross section of the flux rope is deformed, deviating from the cylindrical symmetry approximation and expanding more in the direction perpendicular to the plane of the flux rope axis than in the radial direction. Using the fitting program based on cylindrical symmetry to fit ICMEs with non-cylindrical symmetric cross section may reduce or increase the axial magnetic field.

In this work, we used relatively simple velocity estimation methods, and the lack of plasma data when ICMEs are fitted may cause the radius calculated from the fitting parameters to be too large. However, we believe that the calculated radius is generally relatively large, which does not affect the dependence of the ICME radius on the radial distance. With the launch of China's first Mars mission, Tianwen-1 (Wan et al., 2020), several studies have been conducted to identify the ICME structure at Mars and to investigate the evolution of ICMEs from their eruption to Mars (Chi, Shen, Cheng, et al., 2023; Chi, Shen, Liu, et al., 2023; Ma et al., 2024; H. Zhang et al., 2024). In the future, we will utilize the MOMAG (Liu et al., 2020) data onboard Tianwen-1 to complement our data beyond 1 AU.

Data Availability Statement

The authors thank the Coordinated Data Analysis Web (CDAWeb) (https://cdaweb.gsfc.nasa.gov) for providing the magnetic field and plasma data observed by the MESSENGER, the twin STEREO (including STEREO-A and STEREO-B), the Wind, the Parker Solar Probe, the MAVEN, the Solar Orbiter, and the Ulysses spacecraft/probes. The magnetic field data observed by the VEX and the Juno spacecraft/probes are available through the Planetary Plasma Interactions (PPI) node of the Planetary Data System (PDS) archive (https://pds-ppi.igpp.ucla.edu). The ICMECAT is available from website (https://helioforecast.space/icmecat), and the LineupCAT is available from website (https://helioforecast.space/lineups). We also thank the entire BepiColombo/MPOMAG team for providing data access and support.

Acknowledgments

We acknowledge the use of data from the Mercury Surface, Space Environment, Geochemistry and Ranging (MESSENGER), the Venus Express (VEX), the Solar-Terrestrial Relations Observatory (STEREO), the Wind, the Juno, the Parker Solar Probe (PSP), the Mars Atmosphere and Volatile EvolutioN (MAVEN), the Solar Orbiter (SO), the BepiColombo (Bepi), and the Ulysses satellites. This work is supported by Grants from the NSFC (42325405, 42188101, 42130204, 41904151, 42074222) and the Strategic Priority Program of the Chinese Academy of Sciences (XDB41000000).

References

Amerstorfer, T., Möstl, C., Hess, P., Temmer, M., Mays, M. L., Reiss, M. A., et al. (2018). Ensemble prediction of a halo coronal mass ejection using heliospheric imagers. *Space Weather*, *16*(7), 784–801. https://doi.org/10.1029/2017SW001786

Anderson, B. J., Acuña, M. H., Lohr, D. A., Scheifele, J., Raval, A., Korth, H., & Slavin, J. A. (2007). The magnetometer instrument on MESSENGER. *Space Science Reviews*, *131*(1–4), 417–450. https://doi.org/10.1007/s11214-007-9246-7

Aulanier, G. (2010). What triggers coronal mass ejections. In *38th cospar scientific assembly* (Vol. 38).2.

Bale, S. D., Goetz, K., Harvey, P. R., Turin, P., Bonnell, J. W., Dudok de Wit, T., et al. (2016). The FIELDS instrument suite for solar probe plus. Measuring the coronal plasma and magnetic field, plasma waves and turbulence, and radio signatures of solar transients. *Space Science Reviews*, *204*(1–4), 49–82. https://doi.org/10.1007/s11214-016-0244-5

Bothmer, V., & Schwenn, R. (1998). The structure and origin of magnetic clouds in the solar wind. *Annales Geophysicae*, *16*(1), 1–24. https://doi.org/10.1007/s00585-997-0001-x

Burlaga, L. F. (1988). Magnetic clouds and force-free fields with constant alpha. *Journal of Geophysical Research*, *93*(A7), 7217–7224. https://doi.org/10.1029/JA093iA07p07217

Cargill, P. J. (2004). On the aerodynamic drag force acting on interplanetary coronal mass ejections. *Solar Physics*, *221*(1), 135–149. https://doi.org/10.1023/B:SOLA.0000033366.10725.a2

Chen, J., & Kunkel, V. (2010). Temporal and physical connection between coronal mass ejections and flares. *The Astrophysical Journal*, *717*(2), 1105–1122. https://doi.org/10.1088/0004-637X/717/2/1105

Chi, Y., Shen, C., Cheng, L., Yu, B., Miao, B., Wang, Y., et al. (2023). Interplanetary coronal mass ejections and stream interaction regions observed by Tianwen-1 and maven at mars. *The Astrophysical Journal - Supplement Series*, *267*(1), 3. https://doi.org/10.3847/1538-4365/acd191

Chi, Y., Shen, C., Liu, J., Zhong, Z., Owens, M., Scott, C., et al. (2023). The dynamic evolution of multipoint interplanetary coronal mass ejections observed with BepiColombo, Tianwen-1, and MAVEN. *The Astrophysical Journal Letters*, *951*(1), L14. https://doi.org/10.3847/2041-8213/acd7e7

Chi, Y., Shen, C., Wang, Y., Xu, M., Ye, P., & Wang, S. (2016). Statistical study of the interplanetary coronal mass ejections from 1995 to 2015. *Solar Physics*, *291*(8), 2419–2439. https://doi.org/10.1007/s11207-016-0971-5

Connerney, J. E. P., Benn, M., Bjarno, J. B., Denver, T., Espley, J., Jorgensen, J. L., et al. (2017). The Juno magnetic field investigation. *Space Science Reviews*, *213*(1–4), 39–138. https://doi.org/10.1007/s11214-017-0334-z

Connerney, J. E. P., Espley, J., Lawton, P., Murphy, S., Odom, J., Oliversen, R., & Sheppard, D. (2015). The MAVEN magnetic field investigation. *Space Science Reviews*, *195*(1–4), 257–291. https://doi.org/10.1007/s11214-015-0169-4

Crooker, N., & Intriligator, D. (1996). A magnetic cloud as a distended flux rope occlusion in the heliospheric current sheet. *Journal of Geophysical Research*, *101*(A11), 24343–24348. https://doi.org/10.1029/96JA02129

Davies, E. E., Forsyth, R. J., Winslow, R. M., Möstl, C., & Lugaz, N. (2021). A Catalog of Interplanetary Coronal Mass Ejections Observed by Juno between 1 and 5.4 au. *The Astrophysical Journal*, *923*(2), 136. https://doi.org/10.3847/1538-4357/ac2ccb

Davies, E. E., Winslow, R. M., Scolini, C., Forsyth, R. J., Möstl, C., Lugaz, N., & Galvin, A. B. (2022). Multi-spacecraft Observations of the Evolution of Interplanetary Coronal Mass Ejections between 0.3 and 2.2 au: Conjunctions with the Juno Spacecraft. *The Astrophysical Journal*, *933*(2), 127. https://doi.org/10.3847/1538-4357/ac731a

Démoulin, P., & Dasso, S. (2009). Causes and consequences of magnetic cloud expansion. *Astronomy & Astrophysics*, *498*(2), 551–566. https://doi.org/10.1051/0004-6361/200810971

Ebert, R. W., McComas, D. J., Elliott, H. A., Forsyth, R. J., & Gosling, J. T. (2009). Bulk properties of the slow and fast solar wind and interplanetary coronal mass ejections measured by Ulysses: Three polar orbits of observations. *Journal of Geophysical Research (Space Physics)*, *114*(A1), A01109. https://doi.org/10.1029/2008JA013631

Echer, E., Gonzalez, W. D., Tsurutani, B. T., & Gonzalez, A. L. C. (2008). Interplanetary conditions causing intense geomagnetic storms (Dst < −100 nT) during solar cycle 23 (1996–2006). *Journal of Geophysical Research (Space Physics)*, *113*(A5), A05221. https://doi.org/10.1029/2007JA012744

Fadaaq, M., & Badruddin, B. (2021). Study of transient modulation of galactic cosmic rays due to interplanetary manifestations of coronal mass ejections: 2010–2017. *Astrophysics and Space Science*, *366*(1), 10. https://doi.org/10.1007/s10509-021-03918-6

Farrugia, C. J., Leiter, M., Biernat, H. K., Schwenn, R., Ogilvie, K. W., Matsuil, H., et al. (2005). Evolution of interplanetary magnetic clouds from 0.3 AU to 1 AU: A joint helios-wind investigation. In B. Fleck, T. H. Zurbuchen, & H. Lacoste (Eds.). *Solar wind 11/soho 16, connecting sun and heliosphere*. (Vol. 592), 723

Galvin, A. B., Kistler, L. M., Popecki, M. A., Farrugia, C. J., Simunac, K. D. C., Ellis, L., et al. (2008). The plasma and suprathermal ion composition (PLASTIC) investigation on the STEREO observatories. *Space Science Reviews*, *136*(1–4), 437–486. https://doi.org/10.1007/s11214-007-9296-x

Glassmeier, K. H., Auster, H. U., Heyner, D., Okrafka, K., Carr, C., Berghofer, G., et al. (2010). The fluxgate magnetometer of the BepiColombo Mercury planetary orbiter. *Planetary and Space Science*, *58*(1–2), 287–299. https://doi.org/10.1016/j.pss.2008.06.018

Gold, T., & Hoyle, F. (1960). On the origin of solar flares. *Monthly Notices of the Royal Astronomical Society*, *120*(2), 89–105. https://doi.org/10.1093/mnras/120.2.89

Goldstein, H. (1983). On the field configuration in magnetic clouds. In M. Neugebauer (Ed.), *Nasa conference publication* (Vol. 228, pp. 0–731).

Gonzalez, W. D., Echer, E., Clua-Gonzalez, A. L., & Tsurutani, B. T. (2007). Interplanetary origin of intense geomagnetic storms (Dst < −100 nT) during solar cycle 23. *Geophysical Research Letters*, *34*(6), L06101. https://doi.org/10.1029/2006GL028879

Gonzalez, W. D., Echer, E., Tsurutani, B. T., Clúa de Gonzalez, A. L., & Dal Lago, A. (2011). Interplanetary origin of intense, superintense and extreme geomagnetic storms. *Space Science Reviews*, *158*(1), 69–89. https://doi.org/10.1007/s11214-010-9715-2

Gonzalez, W. D., Joselyn, J. A., Kamide, Y., Kroehl, H. W., Rostoker, G., Tsurutani, B. T., & Vasyliunas, V. M. (1994). What is a geomagnetic storm? *Journal of Geophysical Research*, *99*(A4), 5771–5792. https://doi.org/10.1029/93JA02867

Good, S. W., & Forsyth, R. J. (2016). Interplanetary coronal mass ejections observed by MESSENGER and Venus express. *Solar Physics*, *291*(1), 239–263. https://doi.org/10.1007/s11207-015-0828-3

Good, S. W., Forsyth, R. J., Eastwood, J. P., & Möstl, C. (2018). Correlation of ICME magnetic fields at radially aligned spacecraft. *Solar Physics*, *293*(3), 52. https://doi.org/10.1007/s11207-018-1264-y

Good, S. W., Kilpua, E. K. J., LaMoury, A. T., Forsyth, R. J., Eastwood, J. P., & Möstl, C. (2019). Self-similarity of ICME flux ropes: Observations by radially aligned spacecraft in the inner heliosphere. *Journal of Geophysical Research (Space Physics)*, *124*(7), 4960–4982. https://doi.org/10.1029/2019JA026475

Gopalswamy, N., Lara, A., Lepping, R. P., Kaiser, M. L., Berdichevsky, D., & St. Cyr, O. C. (2000). Interplanetary acceleration of coronal mass ejections. *Geophysical Research Letters*, *27*(2), 145–148. https://doi.org/10.1029/1999GL003639

Gopalswamy, N., Yashiro, S., Kaiser, M. L., Howard, R. A., & Bougeret, J. L. (2001). Radio signatures of coronal mass ejection interaction: Coronal mass ejection cannibalism? *The Astrophysical Journal Letters*, *548*(1), L91–L94. https://doi.org/10.1086/318939

Gosling, J. T., McComas, D. J., Phillips, J. L., Pizzo, V. J., Goldstein, B. E., Forsyth, R. J., & Lepping, R. P. (1995). A CME-driven solar wind disturbance observed at both low and high heliographic latitudes. *Geophysical Research Letters*, *22*(13), 1753–1756. https://doi.org/10.1029/95GL01776

GulisanoF, A. M., Démoulin, P., Dasso, S., & Rodriguez, L. (2012). Expansion of magnetic clouds in the outer heliosphere. *Astronomy & Astrophysics*, *543*, A107. https://doi.org/10.1051/0004-6361/201118748

Halekas, J. S., Taylor, E. R., Dalton, G., Johnson, G., Curtis, D. W., McFadden, J. P., et al. (2015). The solar wind ion analyzer for MAVEN. *Space Science Reviews*, *195*(1–4), 125–151. https://doi.org/10.1007/s11214-013-0029-z

Heyner, D., Auster, H. U., Fornaçon, K. H., Carr, C., Richter, I., Mieth, J. Z. D., et al. (2021). The BepiColombo planetary magnetometer MPO-MAG: What can we learn from the hermean magnetic field? *Space Science Reviews*, *217*(4), 52. https://doi.org/10.1007/s11214-021-00822-x

Horbury, T. S., O'Brien, H., Carrasco Blazquez, I., Bendyk, M., Brown, P., Hudson, R., et al. (2020). The solar orbiter magnetometer. *Astronomy & Astrophysics*, *642*, A9. https://doi.org/10.1051/0004-6361/201937257

Jian, L. K., Russell, C. T., Luhmann, J. G., & Galvin, A. B. (2018). STEREO observations of interplanetary coronal mass ejections in 2007–2016. *The Astrophysical Journal*, *855*(2), 114. https://doi.org/10.3847/1538-4357/aab189

Kasper, J. C., Abiad, R., Austin, G., Balat-Pichelin, M., Bale, S. D., Belcher, J. W., et al. (2016). Solar wind electrons alphas and protons (SWEAP) investigation: Design of the solar wind and coronal plasma instrument suite for solar probe plus. *Space Science Reviews*, *204*(1–4), 131–186. https://doi.org/10.1007/s11214-015-0206-3

Leitner, M., Farrugia, C. J., Möstl, C., Ogilvie, K. W., Galvin, A. B., Schwenn, R., & Biernat, H. K. (2007). Consequences of the force-free model of magnetic clouds for their heliospheric evolution. *Journal of Geophysical Research (Space Physics)*, *112*(A6), A06113. https://doi.org/10.1029/2006JA011940

Lepping, R. P., Jones, J. A., & Burlaga, L. F. (1990). Magnetic field structure of interplanetary magnetic clouds at 1 AU. *Journal of Geophysical Research*, *95*(A8), 11957–11965. https://doi.org/10.1029/JA095iA08p11957

Lepping, R. P., Acũna, M. H., Burlaga, L. F., Farrell, W. M., Slavin, J. A., Schatten, K. H., et al. (1995). The wind magnetic field investigation. *Space Science Reviews*, *71*(1–4), 207–229. https://doi.org/10.1007/BF00751330

Lepping, R. P., Berdichevsky, D. B., Wu, C. C., Szabo, A., Narock, T., Mariani, F., et al. (2006). A summary of WIND magnetic clouds for years 1995-2003: Model-fitted parameters, associated errors and classifications. *Annales Geophysicae*, *24*(1), 215–245. https://doi.org/10.5194/angeo-24-215-2006

Liu, K., Hao, X., Li, Y., Zhang, T., Pan, Z., Chen, M., et al. (2020). Mars orbiter magnetometer of China's first mars mission Tianwen-1. *Earth and Planetary Physics*, *4*(4), 384–389. https://doi.org/10.26464/epp2020058

Liu, Y., Richardson, J. D., & Belcher, J. W. (2005). A statistical study of the properties of interplanetary coronal mass ejections from 0.3 to 5.4 AU. *Planetary and Space Science*, *53*(1–3), 3–17. https://doi.org/10.1016/j.pss.2004.09.023

Liu, Y., Shen, F., & Yang, Y. (2019). Numerical simulation on the propagation and deflection of fast coronal mass ejections (CMEs) interacting with a corotating interaction region in interplanetary space. *The Astrophysical Journal*, *887*(2), 150. https://doi.org/10.3847/1538-4357/ab543e

Lockwood, M., Owens, M. J., Barnard, L. A., Bentley, S., Scott, C. J., & Watt, C. E. (2016). On the origins and timescales of geoeffective IMF. *Space Weather*, *14*(6), 406–432. https://doi.org/10.1002/2016SW001375

Lockwood, M., Owens, M. J., Barnard, L. A., Haines, C., Scott, C. J., McWilliams, K. A., & Coxon, J. C. (2020). Semi-annual, annual and universal time variations in the magnetosphere and in geomagnetic activity: 1. Geomagnetic data. *Journal of Space Weather and Space Climate*, *10*, 23. https://doi.org/10.1051/swsc/2020023

Lugaz, N., Farrugia, C. J., Davies, J. A., Möstl, C., Davis, C. J., Roussev, I. I., & Temmer, M. (2012). The deflection of the two interacting coronal mass ejections of 2010 may 23-24 as revealed by combined in situ measurements and heliospheric imaging. *The Astrophysical Journal*, *759*(1), 68. https://doi.org/10.1088/0004-637X/759/1/68

Lugaz, N., Salman, T. M., Winslow, R. M., Al-Haddad, N., Farrugia, C. J., Zhuang, B., & Galvin, A. B. (2020). Inconsistencies between local and global measures of CME radial expansion as revealed by spacecraft conjunctions. *The Astrophysical Journal*, *899*(2), 119. https://doi.org/10.3847/1538-4357/aba26b

Luhmann, J. G., Curtis, D. W., Schroeder, P., McCauley, J., Lin, R. P., Larson, D. E., et al. (2008). STEREO IMPACT investigation goals, measurements, and data products overview. *Space Science Reviews*, *136*(1–4), 117–184. https://doi.org/10.1007/s11214-007-9170-x

Ma, M., Yang, L., Shen, F., Shen, C., Chi, Y., Wang, Y., et al. (2024). Interplanetary rotation of 2021 december 4 coronal mass ejection on its journey to mars. *The Astrophysical Journal*, *976*(2), 183. https://doi.org/10.3847/1538-4357/ad8a5a

Manchester, W., Gombosi, T., Roussev, I., De Zeeuw, D., Sokolov, I., Powell, K., et al. (2004). Three-dimensional mhd simulation of a flux rope driven cme. *Journal of Geophysical Research*, *109*(A1), A01102. https://doi.org/10.1029/2002JA009672

Markwardt, C. B. (2009). Non-linear least-squares fitting in IDL with MPFIT. In D. A. Bohlender, D. Durand, & P. Dowler (Eds.), *Astronomical data analysis software and systems xviii* (Vol. 411, p. 251). https://doi.org/10.48550/arXiv.0902.2850

McAllister, A. H., Dryer, M., McIntosh, P., Singer, H., & Weiss, L. (1996). A large polar crown coronal mass ejection and a "problem" geomagnetic storm: April 14-23, 1994. *Journal of Geophysical Research*, *101*(A6), 13497–13516. https://doi.org/10.1029/96JA00510

Mierla, M., Inhester, B., Antunes, A., Boursier, Y., Byrne, J. P., Colaninno, R., et al. (2010). On the 3-D reconstruction of Coronal Mass Ejections using coronagraph data. *Annales Geophysicae*, *28*(1), 203–215. https://doi.org/10.5194/angeo-28-203-2010

Möstl, C., Isavnin, A., Boakes, P. D., Kilpua, E. K. J., Davies, J. A., Harrison, R. A., et al. (2017). Modeling observations of solar coronal mass ejections with heliospheric imagers verified with the Heliophysics System Observatory. *Space Weather*, *15*(7), 955–970. https://doi.org/10.1002/2017SW001614

Möstl, C., Weiss, A. J., Bailey, R. L., Reiss, M. A., Amerstorfer, T., Hinterreiter, J., et al. (2020). Prediction of the in situ coronal mass ejection rate for solar cycle 25: Implications for parker solar probe in situ observations. *The Astrophysical Journal*, *903*(2), 92. https://doi.org/10.3847/1538-4357/abb9a1

Möstl, C., Weiss, A. J., Reiss, M. A., Amerstorfer, T., Bailey, R. L., Hinterreiter, J., et al. (2022). Multipoint interplanetary coronal mass ejections observed with solar orbiter, BepiColombo, parker solar probe, wind, and STEREO-A. *The Astrophysical Journal Letters*, *924*(1), L6. https://doi.org/10.3847/2041-8213/ac42d0

Mustajab, F., & Badruddin (2011). Geoeffectiveness of the interplanetary manifestations of coronal mass ejections and solar-wind stream-stream interactions. *Astrophysics and Space Science*, *331*(1), 91–104. https://doi.org/10.1007/s10509-010-0428-5

Ogilvie, K. W., Chornay, D. J., Fritzenreiter, R. J., Hunsaker, F., Keller, J., Lobell, J., et al. (1995). SWE, A comprehensive plasma instrument for the wind spacecraft. *Space Science Reviews*, *71*(1–4), 55–77. https://doi.org/10.1007/BF00751326

Owen, C. J., Bruno, R., Livi, S., Louarn, P., Al Janabi, K., Allegrini, F., et al. (2020). The solar orbiter solar wind analyser (SWA) suite. *Astronomy & Astrophysics*, *642*, A16. https://doi.org/10.1051/0004-6361/201937259

Paularena, K. I., Wang, C., von Steiger, R., & Heber, B. (2001). An ICME observed by Voyager 2 at 58 AU and by Ulysses at 5 AU. *Geophysical Research Letters*, *28*(14), 2755–2758. https://doi.org/10.1029/2001GL013122

Plunkett, S. P., Thompson, B. J., St. Cyr, O. C., & Howard, R. A. (2001). Solar source regions of coronal mass ejections and their geomagnetic effects. *Journal of Atmospheric and Solar-Terrestrial Physics*, *63*(5), 389–402. https://doi.org/10.1016/S1364-6826(00)00166-8

Reisenfeld, D. B., Gosling, J. T., Forsyth, R. J., Riley, P., & St. Cyr, O. C. (2003). Properties of high-latitude CME-driven disturbances during Ulysses second northern polar passage. *Geophysical Research Letters*, *30*(19), 8031. https://doi.org/10.1029/2003GL017155

Richardson, I. G. (2014). Identification of interplanetary coronal mass ejections at Ulysses using multiple solar wind signatures. *Solar Physics*, *289*(10), 3843–3894. https://doi.org/10.1007/s11207-014-0540-8

Richardson, I. G., & Cane, H. V. (2012). Solar wind drivers of geomagnetic storms during more than four solar cycles. *Journal of Space Weather and Space Climate*, *2*, A01. https://doi.org/10.1051/swsc/2012001

Richardson, J. D., Paularena, K. I., Wang, C., & Burlaga, L. F. (2002). The life of a CME and the development of a MIR: From the Sun to 58 AU. *Journal of Geophysical Research (Space Physics)*, *107*(A4), 1041. https://doi.org/10.1029/2001JA000175

Riley, P., & Crooker, N. (2004). Kinematic treatment of coronal mass ejection evolution in the solar wind. *The Astrophysical Journal*, *600*(2, 1), 1035–1042. https://doi.org/10.1086/379974

Riley, P., Linker, J. A., Mikić, Z., Odstrcil, D., Zurbuchen, T. H., Lario, D., & Lepping, R. P. (2003). Using an MHD simulation to interpret the global context of a coronal mass ejection observed by two spacecraft. *Journal of Geophysical Research (Space Physics)*, *108*(A7), 1272. https://doi.org/10.1029/2002JA009760

Russell, C., & Mulligan, T. (2002). The true dimensions of interplanetary coronal mass ejections. In *Advances in Space Research*, S. Gibson & S. Suess (Eds.), Structure, energetics and dynamics of the corona and the heliosphere during the rising phase of the 23rd solar cycle. (E2 2/D2 2 symposium of COSPAR scientific commission E held at the 33rd COSPAR scientific assembly, WARSAW, Poland, JULY, 2000), Vol. 29(3), 301–306. https://doi.org/10.1016/S0273-1177(01)00588-9

Russell, C. T., Shinde, A. A., & Jian, L. (2005). A new parameter to define interplanetary coronal mass ejections. *Advances in Space Research*, *35*(12), 2178–2184. https://doi.org/10.1016/j.asr.2005.04.024

Salman, T. M., Winslow, R. M., & Lugaz, N. (2020). Radial evolution of coronal mass ejections between MESSENGER, Venus express, STEREO, and L1: Catalog and analysis. *Journal of Geophysical Research (Space Physics)*, *125*(1), e27084. https://doi.org/10.1029/2019JA027084

Shen, C., Chi, Y., Wang, Y., Xu, M., & Wang, S. (2017). Statistical comparison of the ICME's geoeffectiveness of different types and different solar phases from 1995 to 2014. *Journal of Geophysical Research (Space Physics)*, *122*(6), 5931–5948. https://doi.org/10.1002/2016JA023768

Shen, C., Wang, Y., Gui, B., Ye, P., & Wang, S. (2011). Kinematic evolution of a slow CME in corona viewed by STEREO-B on 8 october 2007. *Solar Physics*, *269*(2), 389–400. https://doi.org/10.1007/s11207-011-9715-8

Shen, C., Wang, Y., Pan, Z., Miao, B., Ye, P., & Wang, S. (2014). Full halo coronal mass ejections: Arrival at the earth. *Agu fall meeting abstracts*, *2014*, SH43A–4169.

Shen, C., Wang, Y., Wang, S., Liu, Y., Liu, R., Vourlidas, A., et al. (2012). Super-elastic collision of large-scale magnetized plasmoids in the heliosphere. *Nature Physics*, *8*(12), 923–928. https://doi.org/10.1038/nphys2440

Vourlidas, A. (2014). The flux rope nature of coronal mass ejections. *Plasma Physics and Controlled Fusion*, *56*(6), 064001. https://doi.org/10.1088/0741-3335/56/6/064001

Vršnak, B. (2008). Processes and mechanisms governing the initiation and propagation of CMEs. *Annales Geophysicae*, *26*(10), 3089–3101. https://doi.org/10.5194/angeo-26-3089-2008

Vršnak, B., Amerstorfer, T., Dumbović, M., Leitner, M., Veronig, A. M., Temmer, M., et al. (2019). Heliospheric evolution of magnetic clouds. *The Astrophysical Journal*, *877*(2), 77. https://doi.org/10.3847/1538-4357/ab190a

Vršnak, B., Ruždjak, D., Sudar, D., & Gopalswamy, N. (2004). Kinematics of coronal mass ejections between 2 and 30 solar radii. What can be learned about forces governing the eruption? *Astronomy & Astrophysics*, *423*, 717–728. https://doi.org/10.1051/0004-6361:20047169

Vršnak, B., Vrbanec, D., & Čalogović, J. (2008). Dynamics of coronal mass ejections. The mass-scaling of the aerodynamic drag. *Astronomy & Astrophysics*, *490*(2), 811–815. https://doi.org/10.1051/0004-6361:200810215

Vršnak, B., Žic, T., Vrbanec, D., Temmer, M., Rollett, T., Möstl, C., et al. (2013). Propagation of interplanetary coronal mass ejections: The drag-based model. *Solar Physics*, *285*(1–2), 295–315. https://doi.org/10.1007/s11207-012-0035-4

Wan, W. X., Wang, C., Li, C. L., & Wei, Y. (2020). China's first mission to mars. *Nature Astronomy*, *4*(7), 721. https://doi.org/10.1038/s41550-020-1148-6

Wang, C., Du, D., & Richardson, J. D. (2005). Characteristics of the interplanetary coronal mass ejections in the heliosphere between 0.3 and 5.4 AU. *Journal of Geophysical Research (Space Physics)*, *110*(A10), A10107. https://doi.org/10.1029/2005JA011198

Wang, C., & Richardson, J. D. (2004). Interplanetary coronal mass ejections observed by Voyager 2 between 1 and 30 AU. *Journal of Geophysical Research (Space Physics)*, *109*(A6), A06104. https://doi.org/10.1029/2004JA010379

Wang, C., Rosen, I. G., Tsurutani, B. T., Verkhoglyadova, O. P., Meng, X., & Mannucci, A. J. (2016). Statistical characterization of ionosphere anomalies and their relationship to space weather events. *Journal of Space Weather and Space Climate*, *6*, A5. https://doi.org/10.1051/swsc/2015046

Wang, Y., Shen, C., Liu, R., Liu, J., Guo, J., Li, X., et al. (2018). Understanding the twist distribution inside magnetic flux ropes by anatomizing an interplanetary magnetic cloud. *Journal of Geophysical Research (Space Physics)*, *123*(5), 3238–3261. https://doi.org/10.1002/2017JA024971

Wang, Y., Shen, C., Wang, S., & Ye, P. (2004). Deflection of coronal mass ejection in the interplanetary medium. *Solar Physics*, *222*(2), 329–343. https://doi.org/10.1023/B:SOLA.0000043576.21942.aa

Wang, Y., Wang, B., Shen, C., Shen, F., & Lugaz, N. (2014). Deflected propagation of a coronal mass ejection from the corona to interplanetary space. *Journal of Geophysical Research (Space Physics)*, *119*(7), 5117–5132. https://doi.org/10.1002/2013JA019537

Wang, Y., Ye, P., Wang, S., Zhou, G., & Wang, J. (2002). A statistical study on the geoeffectiveness of earth-directed coronal mass ejections from march 1997 to december 2000. *Journal of Geophysical Research*, *107*(A11), SSH2-1–SSH2-9. https://doi.org/10.1029/2002JA009244

Wang, Y., Zhou, Z., Shen, C., Liu, R., & Wang, S. (2015). Investigating plasma motion of magnetic clouds at 1 AU through a velocity-modified cylindrical force-free flux rope model. *Journal of Geophysical Research*, *120*(3), 1543–1565. https://doi.org/10.1002/2014JA020494

Wang, Y., Zhuang, B., Hu, Q., Liu, R., Shen, C., & Chi, Y. (2016). On the twists of interplanetary magnetic flux ropes observed at 1 AU. *Journal of Geophysical Research (Space Physics)*, *121*(10), 9316–9339. https://doi.org/10.1002/2016JA023075

Wenzel, K. P., Marsden, R. G., Page, D. E., & Smith, E. J. (1989). Ulysses: The first high-latitude heliospheric mission. *Advances in Space Research*, *9*(4), 25–29. https://doi.org/10.1016/0273-1177(89)90089-6

Winslow, R. M., Lugaz, N., Philpott, L. C., Schwadron, N. A., Farrugia, C. J., Anderson, B. J., & Smith, C. W. (2015). Interplanetary coronal mass ejections from MESSENGER orbital observations at Mercury. *Journal of Geophysical Research (Space Physics)*, *120*(8), 6101–6118. https://doi.org/10.1002/2015JA021200

Xue, X. H., Wang, Y., Ye, P. Z., Wang, S., & Xiong, M. (2005). Analysis on the interplanetary causes of the great magnetic storms in solar maximum (2000–2001). *Planetary and Space Science*, *53*(4), 443–457. https://doi.org/10.1016/j.pss.2004.10.002

Yu, B., Chi, Y., Owens, M., Scott, C. J., Shen, C., Xue, X., et al. (2023). Tianwen-1 and MAVEN observations of the response of mars to an interplanetary coronal mass ejection. *The Astrophysical Journal*, *953*(1), 105. https://doi.org/10.3847/1538-4357/acdcf8

Yu, B., Scott, C. J., Xue, X., Yue, X., Chi, Y., Dou, X., & Lockwood, M. (2021). A signature of 27 day solar rotation in the concentration of metallic ions within the terrestrial ionosphere. *The Astrophysical Journal*, *916*(2), 106. https://doi.org/10.3847/1538-4357/ac0886

Zhang, H., Shen, F., Yang, Y., Chi, Y., Shen, C., & Tao, X. (2024). Magnetohydrodynamic modeling of background solar wind near mars: Comparison with MAVEN and Tianwen-1. *The Astrophysical Journal*, *971*(2), 151. https://doi.org/10.3847/1538-4357/ad5969

Zhang, J., Dere, K. P., Howard, R. A., & Bothmer, V. (2003). Identification of solar sources of major geomagnetic storms between 1996 and 2000. *The Astrophysical Journal*, *582*(1), 520–533. https://doi.org/10.1086/344611

Zhang, J., Temmer, M., Gopalswamy, N., Malandraki, O., Nitta, N. V., Patsourakos, S., et al. (2021). Earth-affecting solar transients: A review of progresses in solar cycle 24. *Progress in Earth and Planetary Science*, *8*(1), 56. https://doi.org/10.1186/s40645-021-00426-7

Zhang, T., Baumjohann, W., Delva, M., Auster, H. U., Balogh, A., Russell, C. T., et al. (2006). Magnetic field investigation of the Venus plasma environment: Expected new results from Venus Express. *Planetary and Space Science*, *54*(13–14), 1336–1343. https://doi.org/10.1016/j.pss.2006.04.018

Zhao, D., Guo, J., Huang, H., Lin, H., Hong, Y., Feng, X., et al. (2021). Interplanetary coronal mass ejections from maven orbital observations at mars. *The Astrophysical Journal*, *923*(1), 4. https://doi.org/10.3847/1538-4357/ac294b